A Uniform Retrieval Analysis of Ultra-cool Dwarfs. IV. A Statistical Census from 50 Late T-dwarfs

by

Kezman Saboi

A Thesis Presented in Partial Fulfillment
of the Requirement for the Degree
Master of Science

Approved November 2020 by the
Graduate Supervisory Committee:

Michael Line, Chair
Jennifer Patience
Patrick Young

ARIZONA STATE UNIVERSITY

December 2020

ABSTRACT

The spectra of brown dwarfs are key to exploring the chemistry and physics that take place in their atmospheres. Late T dwarf (950 - 500 K) spectra are particularly diagnostic due to their relatively cloud free atmospheres and deep molecular bands. With the use of powerful atmospheric retrieval tools, these properties permit constraints on molecular/atomic abundances and temperature profiles. Building upon previous analyses on T and Y dwarfs (Line et al. 2017; Zalesky et al. 2019), I present a uniform retrieval analysis of 50 T dwarfs via their low-resolution near-infrared spectra. This analysis more than doubles the sample of T dwarfs with retrieved properties. I present updates on current compositional trends and thermal profile constraints amongst the T dwarf population. My analysis shows that my collection of objects form trends that are consistent with solar grid model expectations for water, ammonia, methane, and potassium. I also establish a consistency between the thermal structures of my objects with those of grid models. Moreover, I explore the origin of gravity-metallicity discrepancies that are observed in some of my brown dwarf candidates.

DEDICATION

I dedicate this work to my parents, Mulele and Monde Florence Saboi, the rest of my family, and everyone else along the path of my education who has contributed to getting me to where I am today. Indeed, it takes a village to raise a child.

ACKNOWLEDGEMENTS

Firstly, I would like to express my deep gratitude to my advisor, Prof. Michael Line, for taking a chance in me by affording me the opportunity to work with him. His tremendous support just before and throughout my graduate studies encouraged me to not only work hard but also maintain my focus on performing my research work. I would also like to thank my supervisory committee members, Prof. Jennifer Patience and Prof. Patrick Young, for all the great support and encouragement they rendered to me. A lot of my gratitude also goes to fellow students and colleagues who include Dr. Adam Schneider, Joseph Zalesky, and Aishwarya Iyer. Lastly, but not the least, I would like to acknowledge and thank my research collaborators Zhoujian Zhang, Michael C. Liu, William M. J. Best, and Mark S. Marley.

A majority of the T-dwarf data in this investigation were obtained with the NASA IRTF SpeX instrument Rayner *et al.* (2003) under proposals 2017A115, 2017B087, 2018B128 (PI M. Liu) . The retrieval analysis work is supported by the National Science Foundation under Grant No. 1615220. This research has benefited from the SpeX Prism Spectral Libraries, maintained by Adam Burgasser at this http://pono.ucsd.edu/ adam/browndwarfs/spexprismlink. The research shown herein acknowledges use of the Hypatia Catalog Database, an online compilation of stellar abundance data as described in Hinkel *et al.* (2014).

TABLE OF CONTENTS

LIST OF TABLES

Table Page

LIST OF FIGURES

Chapter 1

INTRODUCTION

1.1 Background

Brown dwarfs are substellar objects whose masses are intermediate between the latest M-type stars and the most massive planets (Hayashi and Nakano, 1963; Shu, 1977; Becklin and Zuckerman, 1988; Rebolo *et al.*, 1995; Oppenheimer *et al.*, 1995; Saumon *et al.*, 2006). Similar to stars, brown dwarfs are hypothesized to form from interstellar molecular gas cloud core collapse (Uehara and Inutsuka, 2000; Bate *et al.*, 2002; Krumholz *et al.*, 2005; Whitworth and Stamatellos, 2006; Chabrier *et al.*, 2007; Whitworth *et al.*, 2007; Hennebelle, 2012), but do not achieve masses high enough to sustain core H-fusion over their lifetime (Burrows *et al.*, 2001). As the effective temperatures of brown dwarfs are much lower than those of stars (< 2500K), they tend to form molecules and condensates that in turn dominate the spectral energy distribution, resulting in atmospheres that are more planetary than stellar. It is through analyses of their spectra that I are able to infer the nature of brown dwarfs, how they evolve overtime, and hence I are able to use them as great atmospheric "process" laboratories.

Some key properties of brown dwarfs include their mass, radius, gravity, effective temperatures ($T_{\rm eff}$), and elemental abundances (see review in Marley and Robinson 2015; Kirkpatrick 2005). Robust masses are usually derived through dynamical means (Dupuy and Liu, 2012) and radius is inferred via distance and bolometric luminosity. Determining gravity, effective temperatures, and abundances for brown dwarfs can be more challenging than it is for stars due to the lack of clear "atomic lines" for which classic single or multi-line spectral analyses can be performed. As such, models play a more important role in these determinations.

A common modeling approach for determining these properties from their spectra is through comparisons to grids of model spectra computed with self-consistent one-dimensional radiative-convective equilibrium models (e.g., Allard *et al.* 1996; Marley *et al.* 1996; Burrows *et al.* 2001), akin to classic stellar atmosphere modeling. This approach typically relies upon the use of a-priori chemical/physical assumptions such as thermochemical equilibrium molecular/atomic abundances and 1D radiative-convective equilibrium (Burrows et al. 2001, Marley and Robinson 2016). These assumptions reduce the dimensionality of the inference problem to just a handful of parameters such as T_{eff}, log$g$, and a composition parameter like metallicity $[M/H]$ (in some cases alpha-element enhancement, e.g., Huesser et al.). A few key issues arise with such a method. First, the low model dimensionality restricts any inference solely to the dimensions specified for the pre-computed grid. Second, the choice of inference tool is often not rigorous and typically does not account for grid-interpolation uncertainties (e.g., often a simple chi-square type minimizer is combined with a multi-linear-type interpolater) and can result in artificially precise constraints. Thirdly, often times the overly restrictive assumptions lead to poor model spectra fits to the data (e.g., Patience *et al.* (2012)), leading one to question the validity of the self-consistent modeling assumptions. Recently, Zhang et al. 2020a,b (submitted) sought to remedy the second and third issues through the use of a modernized self-consistent grid (Marley et al. 2020, in prep) combined with the `Starfish` tool (Czekala *et al.* (2015)), which attempts to marginalize over the finite model grid spacing, interpolation uncertainties, and data-model misfits. However, such an approach is still restricted to a-priori physical assumptions within the grid.

A recently utilized, more flexible alternative, known as "atmospheric retrieval", has shown success in providing constraints and good model-data fits to low resolution spectral observations of T-dwarfs (Line *et al.*, 2014, 2015). Originally developed to determine tempertaures/abundances from spectral soundings of the Solar System planets (Fletcher *et al.*, 2007; Irwin *et al.*, 2008; Greathouse *et al.*, 2011), this technique relies on the use of forward radiative transfer model that relaxes many of the self-consistent grid model assumptions at the expense of many free parameters, combined with a parameter estimation tool (e.g., Levenberg-Marquarted, Markov-Chain Monte Carlo). The fundamental philosophy of the retrieval approach, in contrast to the grid approach, is that much of the fundamental physical/chemical mechanisms operating in, at least, planetary atmospheres, are not understood well enough to build accurate enough fully self-consistent models. The aim is to directly determine, from the spectra, the vertical temperature profiles and abundance composition. This approach has recently become rather prolific in the extra-solar planet atmosphere field (e.g., see review by Madhusudhan (2019)).

Recognizing the shortcomings of the grid-fitting/modeling approach, and the potential advantages of the atmospheric retrieval method, Line *et al.* (2015) applied the atmospheric retrieval approach to low resolution SpeX data of the benchmark late T-dwarfs, Gl 570D and HD 3651B. Late dwarfs were specifically chosen to mitigate the impact of uncertain cloud properties and the presentation of strong molecular absorption features from water and methane. Using radiative transfer forward model with ∼30 free parameters combined with a Markov chain Monte Carlo (Foreman-Mackey *et al.*, 2013), they were able to obtain bounded constraints on the molecular mixing ratios for H_2O, CH_4, NH_3 and $Na+K$, the vertical thermal profiles (temperature vs. pressure), gravity, and photometric radii (given the parallactic distances). The key findings were 1) the ammonia abundance could be constrained from low-resolution near-infrared spectra alone, a surprise given the lack of obvious spectral features (typical of longer wavelengths Saumon *et al.* 2006 or higher resolutions (Canty *et al.*, 2015)), 2) the retrieved molecular (and alkali) abundances were consistent with self-consistent chemical predictions (albeit constant-with-altitude mixing ratios were assumed in the retrieval) 3) derived metallicities and carbon-to-oxygen ratios were consistent with their host star abundances, and 4) the vertical thermal temperature profiles agreed with radiative (convective)-equilibrium expectations. Taken together, these findings lend support that the retrieval paradigm can be used as a complimentary tool to grid-modeling for inferring fundamental brown dwarf atmospheric properties.

Having validated the retrieval methodology against late-T benchmark systems, Line *et al.* (2017) performed a systematic retrieval analysis on the spectra of 11 late T-dwarfs (T7-T8, spanning 600 - 800K) available in the SpeX prism library (Burgasser, 2014). This uniform analysis found that 1) the large number of free parameters required in retrievals, compared to self-consistent grid models (27 vs. 4 parameters), is justified owing to their much better fits, 2) the T7/T8 atmospheres are cloud free (upper limits on the cloud optical depth of unity were obtained), 3) the temperature profiles for all objects were consistent with radiative-convective equilibrium expectations, 4) the retrieved gravities, radii, and inferred effective temperatures agreed with evolution model predictions, 5) abundances for ammonia, methane, and water were found to be constant with effective temperature but a strong decreasing trend in the alkali abundances was observed to occur with decreasing effective temperature, and 6) the late T-dwarf ensemble had somewhat lower metallicities and higher carbon-to-oxygen ratios than the local FGK stellar population. These findings provided a first look at the carbon-to-oxygen ratio and metallicities of a sample brown dwarfs as well as the first direct determination of the possible influence of alkali rainout on their abundances.

Building upon Line *et al.* (2015, 2017), Zalesky *et al.* (2019) extended the uniform retrieval analysis into the cooler Y-dwarfs. This sampled comprised eleven Y dwarfs and three T dwarfs as observed with the *Hubble Space Telescope*'s Wide Field Camera 3 (WFC3) (Schneider *et al.*, 2015). Their conclusions were similar to the late-T results Line *et al.* (2017), finding that 1) the retrieved temperature profiles for most objects were consistent with radiative-convective equilibrium predictions, 2) water and methane abundances were consistent equilibrium chemistry, 3) the ammonia abundances showed an upward rise with decreasing temperature, with scatter consistent with both equilibrium and quenched abundances, 4) constraints and/or upper limits on the alkali abundances consistent with rain-out predictions, 5) very high gravities, pushing the limits of the evolution models, and 6) elemental abundance ratios broadly inline with those from the local FGK star population. They also compared the results of a self-consistent grid fit to the retrieval results finding that 1) the retrievals fit better and the large number of free parameters were justified, and 2) constraints on common parameters (T_{eff}, log$g$, metallicity, and radius) were outside of each-others 1-sigma uncertainties.

Additional works by Burningham et al. 2017 and Gonzolaz et al. 2020 focused on determining the fundamental properties of L-dwarfs using similar retrieval methods. L-dwarfs are more complicated due to the presence of clouds and additional higher temperature species (hydrides, oxides), and the reduced vertical grasp on the thermal structures. Overall these cloudy investigations showed that the retrieved temperature structures could be degenerate with the presence of clouds, but that plausible abundances of the hydrides/oxides could be retrieved, opening up the possibility of abundance determinations at higher temperatures.

In this work, I extend the late-T analysis in Line *et al.* (2017) to a broader sample of 50 T7-T9-dwarfs with were most recently found in a volume limited survey (Best *et al.* (2020)). These objects were then followed up IRTF SpeX spectra (Zhang et al. 2020a,b). This investigation represents the largest uniform retrieval analysis on a nearly complete sample of late T-dwarfs, a factor of 5 over the analysis in Line *et al.* (2017). Again, as in the past works of this series, I focus on late T-dwarfs as these have been shown to be largely free of influence from clouds and they present deep methane and water absorption features, enabling simultaneous carbon and oxygen constraints.

I follow closely the methodologies and analysis as in Line *et al.* (2017) and Zalesky *et al.* (2019). In Section 2, I briefly discuss the source of the data and review the retrieval methodology. Section 3 presents the retrieved constraints for the thermal structures (3.1), composition (3.2), and evolutionary parameters (3.3). I discuss these results in section 4, and finally summarize the findings in section 5.

1.2 Data

I focus on IRTF SpeX prism observations (0.95 - 2.5 μm, R$\sim$120) of the late-T dwarf described in Zhang et al. 2020b (submitted) (see their Table 3). There are a total of 55 objects with SpeX spectra with 39 available within the SpeX Prism Library (Burgasser 2006a, Burgasser and the Splat Development Team 2017) and 16 from an observational campaign (through IRTF programs 2017A115, 2017B087, 2018B128– Zhang et al. 2020). Briefly, the sample is comprised of the late-T dwarfs from the volume limited (<25 pc) survey in Best et al. 2018 with the SpeX objects out to 20 pc. 54 of the 55 have well measured parallax's and all spectra are flux calibrated using MKO H-band photometry (Table 1.1). Figure 1.1) provides the color (J vs. J-K) context for the sample. The analysis, for uniformity purposes, also includes the 11 objects from Line *et al.* (2017). Due to low signal-to-noise, the final analysis excludes 5 objects, for a total of 50 in the analysis. As in the past works, I only keep every other 3rd point as SpeX samples the line-spread shape with ∼ 2.5 pixels. This is performed to minimize the over-fitting of data.

Table 1.1: Basic properties of the 50 targets

Name of Object	Spec. Type	J_{MKO} [mag]	H_{MKO} [mag]	K_{MKO} [mag]	Distance [pc]
SDSS J162838.77+230821.1	T7	$16.25^{+0.03}_{-0.03}$	$16.72^{+0.03}_{-0.03}$	$16.63^{+0.03}_{-0.03}$	$13.32^{+0.16}_{-0.16}$ **(2)**
WISE J112438.12-042149.7	T7	$16.72^{+0.13}_{-0.13}$	16.37	16.32	$17.39^{+0.10}_{-0.10}$ **(1)**
WISE J004945.61+215120.0PRZ0.5	T8	$17.63^{+0.13}_{-0.13}$	$18.09^{+0.14}_{-0.14}$	$18.06^{+0.14}_{-0.14}$	$24.81^{+1.48}_{-1.48}$ **(3)**
WISEPC J222623.05+044003.9	T8	$16.90^{+0.02}_{-0.02}$	$17.24^{+0.09}_{-0.09}$	$17.45^{+0.07}_{-0.07}$	$18.38^{+1.99}_{-1.99}$ **(3)**
WISE J105257.95-194250.2	T7.5	$16.84^{+0.02}_{-0.02}$	$16.99^{+0.06}_{-0.06}$	$17.07^{+0.06}_{-0.06}$	$14.73^{+0.48}_{-0.48}$ **(1)**
UGPS J052127.27+364048.6	T8.5	$16.94^{+0.02}_{-0.02}$	$17.32^{+0.09}_{-0.09}$	$17.28^{+0.04}_{-0.04}$	$8.18^{+0.11}_{-0.11}$ **(3)**
WISEPC J221354.69+091139.4	T7	$16.77^{+0.02}_{-0.02}$	$17.12^{+0.06}_{-0.06}$	$17.11^{+0.06}_{-0.06}$	$19.19^{+1.14}_{-1.14}$ **(1)**
WISE J200050.19+362950.1	T8	$15.44^{+0.01}_{-0.01}$	$16.13^{+0.04}_{-0.04}$	$15.85^{+0.01}_{-0.01}$	$7.62^{+0.17}_{-0.17}$ **(1)**
WISE J004024.88+090054.8	T7	$16.13^{+0.01}_{-0.01}$	$16.56^{+0.02}_{-0.02}$	$16.55^{+0.05}_{-0.05}$	$14.01^{+0.53}_{-0.53}$ **(1)**
2MASS J00501994-3322402	T7	$15.65^{+0.1}_{-0.1}$	$16.04\ ^{+0.1}_{-0.1}$	$15.91^{+0.1}_{-0.1}$	$10.57^{+0.27}_{-0.27}$ **(2)**
WISEPA J012333.21+414203.9	T7	$17.00^{+0.02}_{-0.02}$	$17.29^{+0.06}_{-0.06}$	$17.29^{+0.06}_{-0.06}$	$25.38^{+1.55}_{-1.55}$ **(1)**
WISE J024124.73-365328.0	T7	$16.59^{+0.04}_{-0.04}$	$17.04^{+0.07}_{-0.07}$	N/A	$19.08^{+0.98}_{-0.98}$ **(3)**
WISE J032547.72+083118.2	T7	$16.29^{+0.07}_{-0.07}$	$16.19^{+0.08}_{-0.08}$	$16.39^{+0.09}_{-0.09}$	$12.74^{+0.49}_{-0.49}$ **(3)**
WISE J061437.73+095135.0	T7	$16.43^{+0.02}_{-0.02}$	$16.64^{+0.06}_{-0.06}$	$16.49^{+0.06}_{-0.06}$	$17.61^{+0.62}_{-0.62}$ **(1)**
2MASSI J0727182+171001	T7	$15.19^{+0.03}_{-0.03}$	$15.67^{+0.03}_{-0.03}$	$16.69^{+0.03}_{-0.03}$	$8.89^{+0.07}_{-0.07}$ **(2)**
WISE J125448.52-072828.4	T8	$17.3^{+0.01}_{-0.01}$	$17.63^{+0.03}_{-0.03}$	$17.39^{+0.07}_{-0.07}$	$24.21^{+1.58}_{-1.58}$ **(1)**
WISE J125715.90+400854.2	T7	$16.88^{+0.02}_{-0.02}$	$17.12^{+0.06}_{-0.06}$	$17.16^{+0.07}_{-0.07}$	$17.51^{+0.55}_{-0.55}$ **(1)**
WISEPC J145715.03+581510.2	T7	$16.82^{+0.02}_{-0.02}$	$17.16^{+0.06}_{-0.06}$	$17.22^{+0.07}_{-0.07}$	$21.41^{+2.61}_{-2.61}$ **(1)**
PSO J224.3820+47.4057	T7	$17.1^{+0.02}_{-0.02}$	$17.43\ ^{+0.06}_{-0.06}$	$17.06^{+0.06}_{-0.06}$	$20.2^{+1.22}_{-1.22}$ **1**

SDSS J150411.63+102718.4	T7	$16.51^{+0.01}_{-0.01}$	$16.99^{+0.05}_{-0.05}$	$17.12^{+0.08}_{-0.08}$	$21.69^{+0.71}_{-0.71}$ **(2)**
2MASSI J1553022+153236	T7	$15.34^{+0.03}_{-0.03}$	$15.76^{+0.03}_{-0.03}$	$15.94^{+0.03}_{-0.03}$	$13.32^{+0.16}_{-0.16}$ ((2))
WISEPC J215751.38+265931.4	T7	$17.05^{+0.02}_{-0.02}$	$17.49^{+0.04}_{-0.04}$	$17.34^{+0.06}_{-0.06}$	$15.92^{+0.56}_{-0.56}$ **(1)**
WISEPC J220922.10-273439.5	T7	$16.6^{+0.02}_{-0.02}$	$16.95^{0.06+}_{-0.06}$	$17.35^{+0.06}_{-0.06}$	$13.81^{+0.72}_{-0.72}$ **(1)**
WISEPC J234026.62-074507.2	T7	$16.08^{+0.03}_{-0.03}$	$16.4^{+0.03}_{-0.03}$	$16.51^{+0.06}_{-0.06}$	$20.92^{+1.36}_{-1.36}$ **(3)**
WISEPC J234841.10-102844.4	T7	$16.63^{+0.02}_{-0.02}$	$16.99^{+0.06}_{-0.06}$	$16.84^{+0.06}_{-0.06}$	$14.79^{+0.83}_{-0.83}$ **(1)**
HD3651B	T7.5	$16.16^{+0.03}_{-0.03}$	$16.68^{+0.04}_{-0.04}$	$16.87^{+0.05}_{-0.05}$	$11.14^{+0.01}_{-0.01}$ **(4)**
WISEPC J022322.39-293258.1	T7.5	$17.1^{+0.05}_{-0.05}$	$17.3^{+0.11}_{-0.11}$	$17.59^{+0.08}_{-0.08}$	$12.39^{+0.4}_{-0.4}$ **(3)**
WISE J052126.29+102528.4	T7.5	$14.86^{+0.02}_{-0.02}$	$15.25^{+0.06}_{-0.06}$	$14.98^{+0.06}_{-0.06}$	$7.07^{+0.25}_{-0.25}$ **(1)**
WISE J103907.73-160002.9	T7.5	$16.95^{+0.02}_{-0.02}$	$17.19^{+0.04}_{-0.04}$	$17.1^{+0.07}_{-0.07}$	$22.12^{+0.93}_{-0.93}$ **(1)**
2MASS J11145133-2618235	T7.5	$15.52^{+0.05}_{0.05-}$	$15.82^{+0.05}_{-0.05}$	$16.54^{+0.05}_{-0.05}$	$5.58^{+0.04}_{-0.04}$ **(2)**
2MASSI J1217110-031113	T7.5	$15.56^{+0.03}_{-0.03}$	$15.98^{+0.03}_{-0.03}$	$15.92^{+0.03}_{-0.03}$	$10.91^{+0.26}_{-0.26}$ **(5),(3)**
ULAS J141623.94+134836.3	(sd)T7.5	$17.26^{+0.02}_{-0.02}$	$17.58^{+0.03}_{-0.03}$	$18.43^{+0.08}_{-0.08}$	$9.3^{+0.03}_{-0.03}$ **(4)**
Gliese 570D	T7.5	$14.82^{+0.05}_{-0.05}$	$15.28^{+0.05}_{-0.05}$	$15.52^{+0.05}_{-0.05}$	5.88 **(4)**
WISEPC J231939.13-184404.3	T7.5	$17.56^{+0.02}_{-0.02}$	$17.95^{+0.05}_{-0.05}$	$18.26^{+0.08}_{-0.08}$	$11.75^{+0.43}_{-0.43}$ **(1)**
ULAS J232123.79+135454.9	T7.5	$16.72^{+0.03}_{-0.03}$	$17.15^{+0.03}_{-0.03}$	$17.16^{+0.01}_{-0.01}$	$11.96^{+0.34}_{-0.34}$ **(3)**
WISEPA J185215.78+353716.3	T7	$16.33^{+0.02}_{-0.02}$	$16.72^{+0.06}_{-0.06}$	$16.5^{+0.06}_{-0.06}$	$15.06^{+0.66}_{-0.66}$
PSO J043.5395+02.3995	T8	$15.92^{+0.01}_{-0.01}$	$16.29^{+0.02}_{-0.02}$	$16.73^{+0.05}_{-0.05}$	$6.84^{+0.07}_{-0.07}$ **(3)**
2MASSI J0415195-093506	T8	$15.32^{+0.03}_{-0.03}$	$15.7^{+0.03}_{-0.03}$	$15.83^{+0.03}_{-0.03}$	$5.71^{+0.06}_{-0.06}$ **(2)**
2MASS J07290002-3954043	T8pec	$15.66^{+0.08}_{-0.08}$	$16.05^{+0.1}_{-0.1}$	$16.5^{+0.1}_{-0.1}$	$7.92^{+0.52}_{-0.52}$ **(8)**

2MASS J09393548-2448279	T8	$15.61^{+0.09}_{-0.09}$	$15.96^{+0.09}_{-0.09}$	$16.83^{+0.09}_{-0.09}$	$5.34^{+0.13}_{-0.13}$ **(7)**
ULAS J102940.52+093514.6	T8	$17.28^{+0.01}_{-0.01}$	$17.63^{+0.01}_{-0.01}$	$17.64^{+0.02}_{-0.02}$	$14.6^{+0.36}_{-0.36}$ **(1)**
Ross 458C	T8	$16.69^{+0.02}_{-0.02}$	$17.01^{+0.04}_{-0.04}$	$16.9^{+0.06}_{-0.06}$	$11.51^{+0.02}_{-0.02}$ **(4)**
WISEPA J132233.66-234017.1	T8	$16.75^{+0.11}_{-0.11}$	$16.65^{+0.14}_{-0.14}$	$17.02^{+0.4}_{-0.4}$	$12.9^{+0.7}_{-0.7}$ **(3)**
WISEPA J165311.05+444423.9	T8	$17.07^{+0.02}_{-0.02}$	$17.59^{+0.05}_{-0.05}$	$17.05^{+0.07}_{-0.07}$	$13.21^{+0.33}_{-0.33}$ **(3)**
WISEPA J171104.60+350036.8PRZ0.5	T8	$17.63^{+0.13}_{-0.13}$	$18.06^{+0.14}_{-0.14}$	$18.09^{+0.14}_{-0.14}$	$24.81^{+1.48}_{-1.48}$ **(3)**
WISE J181329.40+283533.3	T8	$16.92^{+0.02}_{-0.02}$	$17.11^{+0.06}_{-0.06}$	$16.92^{+0.06}_{-0.06}$	$13.59^{+0.37}_{-0.37}$ **(1)**
WISEPA J195905.66-333833.7	T8	$16.71^{+0.07}_{-0.07}$	$17.18^{+0.05}_{-0.05}$	$16.93^{+0.09}_{-0.09}$	$11.72^{+0.3}_{-0.3}$ **(3)**
WISEPC J225540.74-311841.8	T8	$17.33^{+0.01}_{-0.01}$	$17.66^{+0.03}_{-0.03}$	$17.42^{+0.05}_{-0.05}$	$14.14^{+0.84}_{-0.84}$ **(3)**
WISEPA J045853.89+643452.9	T8.5	$17.13^{+0.07}_{-0.07}$	$17.45^{+0.11}_{-0.11}$	$17.74^{+0.1}_{-0.1}$	$9.16^{+0.3}_{-0.3}$ **(3)**
WISEPA J174124.26+255319.5	T9	$16.18^{+0.02}_{-0.02}$	$16.31^{+0.04}_{-0.04}$	$17.02^{+0.2}_{-0.2}$	$4.67^{+0.06}_{-0.06}$ **(3)**

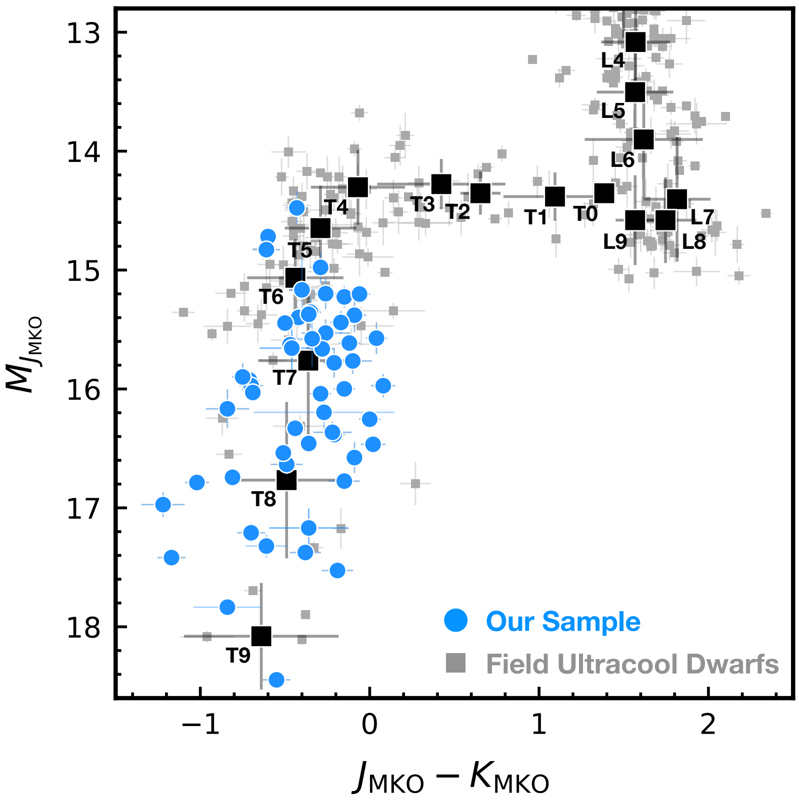

Figure 1.1: An MKO system based color-magnitude diagram of a population of field brown dwarfs ((Best *et al.*, 2018, 2020)), and a collection of brown dwarfs from this study. This collective ensemble shows L and T dwarfs, in descending order from the top of the diagram to the bottom.

Chapter 2

METHODS

The retrieval framework follows closely that described in Line *et al.* (2017) and Zalesky *et al.* (2019), with a few minor modifications. I separate the alkali's into both Na and K (as opposed to Na+K), removed H_2S, and updated the alkali metal wing profiles (Allard et al. 2016)–all other opacity sources are identical to what's in Line *et al.* (2017) and Zalesky *et al.* (2019)). Cross-section sampling is used at a constant R=10000 (vs. 1 cm-1 resolution), a resolution sufficient for interpreting SpeX brown dwarf observations (Line *et al.*, 2015). The remaining parameters are given in Table 2.1 (for a total of 31 free parameters). In the table, note that 16 of the 31 parameters are accounted for by temperatures a different layers (slabs) of an atmosphere. Parameter prior ranges are the same as those in Table 2 of Line *et al.* (2015) with subsequent modifications in Line *et al.* (2017) and Zalesky *et al.* (2019). Fits were assessed using the likelihood function given by equation 2 in parameter estimation (utilizing the likelihood function in Line *et al.* (2015)) was performed with the `emcee` package (Foreman-Mackey *et al.*, 2013) with 224 walkers run out to 60,000 iterations. I ran a few test case's out to between 120K and 1 million iterations and found no significant differences from 60K. `emcee`, like all MCMC-based methods, requires an initial guess to initiate the walkers. The initial guess is based on a "gaussian-ball" about a lose "by hand" fit to the spectra of each object. The solutions are insensitive to the intial guess.

Due to the larger number of objects, to reduce computational burden, I had to re-write the core radiative transfer solver (relations in appendix A in Lacis & Oinas 1991) to make use of graphics processing units (GPUs). This was done using the

Anaconda Numba guvectorize framework on NVIDIA Tesla V100 GPUs. Forward model times improved by a factor of $\sim$ 100 (0.01s or so per model, at an R=10,000 over the 0.95 - 2.5 wavelength range). Given the limited memory of the GPUs (32 GB), I could only run up to 16 simultaneous CPU threads at a time. The overall computational improvement between this work and in Line *et al.* (2017) is about a factor of 10 (about 6 hours to hit 60,000 iterations). GPU and CPU routines produced identical model spectra and thus had no impact on any science results.

Table 2.1: Retrieved Parameters

Parameter	Description
$\log(f_i)$	log of the Volume Mixing Ratio (VMR) of a gas species that is constant with altitude. Gases that are considered include H_2O, CH_4, CO, CO_2, NH_3, K, and Na
$\log(g)$	log of surface gravity [cm s^2]
$(R/D)^2$	Radius-to-distance scale factor [$R_{\rm Jup}$/pc]
T_i	Temperature (in Kelvin) at a given pressure level
$\Delta\lambda$	Wavelength calibration uncertainty [nm]
b	errorbar inflation exponent
γ	TP-profile smoothing hyperparameter (eq. 5, Line *et al.* (2015))
κ_{P_0}, P_0, α	Cloud opacity profile parameters (cloud base opacity, cloud base pressure, cloud fractional scale height)

Chapter 3

RESULTS

As it is unwieldy, and largely un-informative, to show the full posteriors and discuss each individual object (those are made available online at ZENODO link), here we simply summarize the key results broken down by thermal structure, composition (molecular abundance trends/chemistry and elemental abundances), and evolutionary-like parameters.

Figures 3.1 and 3.2 provide a snap shot of the fits and temperature-pressure profiles, respectively, of a sub-sample of representative objects. The best fits and temperature profiles for all objects in the sample are provided in the appendix (Figures B.1 and C.1). Table A.1 summarizes the nominal constraints for the key properties of individual objects. As in the past works, the effective temperatures are derived by integrating over an ensemble of best fits for each object, extrapolated out to between 0.7 - 100 , and radius is derived from the retrieved $(R/D)^2$ scale factor and the measured distances (from Table 1.1). The elemental abundances are derived from the retrieved molecular abundances (more details below). When comparing the retrieved quantities to those predicted from "self-consistent" grids (given an effective temperature and gravity and assuming solar abundance chemistry and cloud free), I refer to those produced by the ScCHIMERA model described/developed in Piskorz et al. 2018; Arcangeli et al. 2018; Gharib-Nezhad & Line 2019 and used for the same purposes as in Zalesky et al. 2019.

3.1 Thermal Structures

The vertical temperature structure of any atmosphere is a basic atmospheric quantity/property that is required for understanding atmospheric energy balance and chemistry. The temperature profile shape dictates the importance specific chemical mechanisms and determines where clouds ultimately form in an atmosphere. It is generally presumed (Marley and Robinson, 2015), and indeed demonstrated (Line *et al.*, 2015, 2017; Zalesky *et al.*, 2019), that radiative-convective equilibrium dictates the equilibrium thermal structure, set by the effective temperature, gravity and opacity structure (which dictates the optical depth-pressure relationship). Typically, for brown dwarfs, this results in a monotonically decreasing temperature with pressure and radiative-convective boundaries predicted to occur between a few bars to ~ 100 bars. Detached convection zones are also predicted to occur for effective temperatures $> 1500K$, usually arising from the induced temperature gradients driven by cloud formation (Burrows et al. 2006).

Figure 3.2 summarizes the general morphology of the thermal structures for 9 representative objects, compared to those arising from several self-consistent radiative-convective model assumptions. In general, the temperatures monotonically decreases with decreasing pressure, as expected.

3.2 Atmospheric Composition

3.2.1 Molecular Abundances

Photospheres of T-dwarfs are rich with various molecules. As alluded to earlier, much of my focus is placed on understanding the molecular abundance trends of the ensemble of brown dwarfs for H_2O, CH_4, NH_3, and K constrained species. I emphasize these gases because they are the most traceable gases in the probed wavelength range

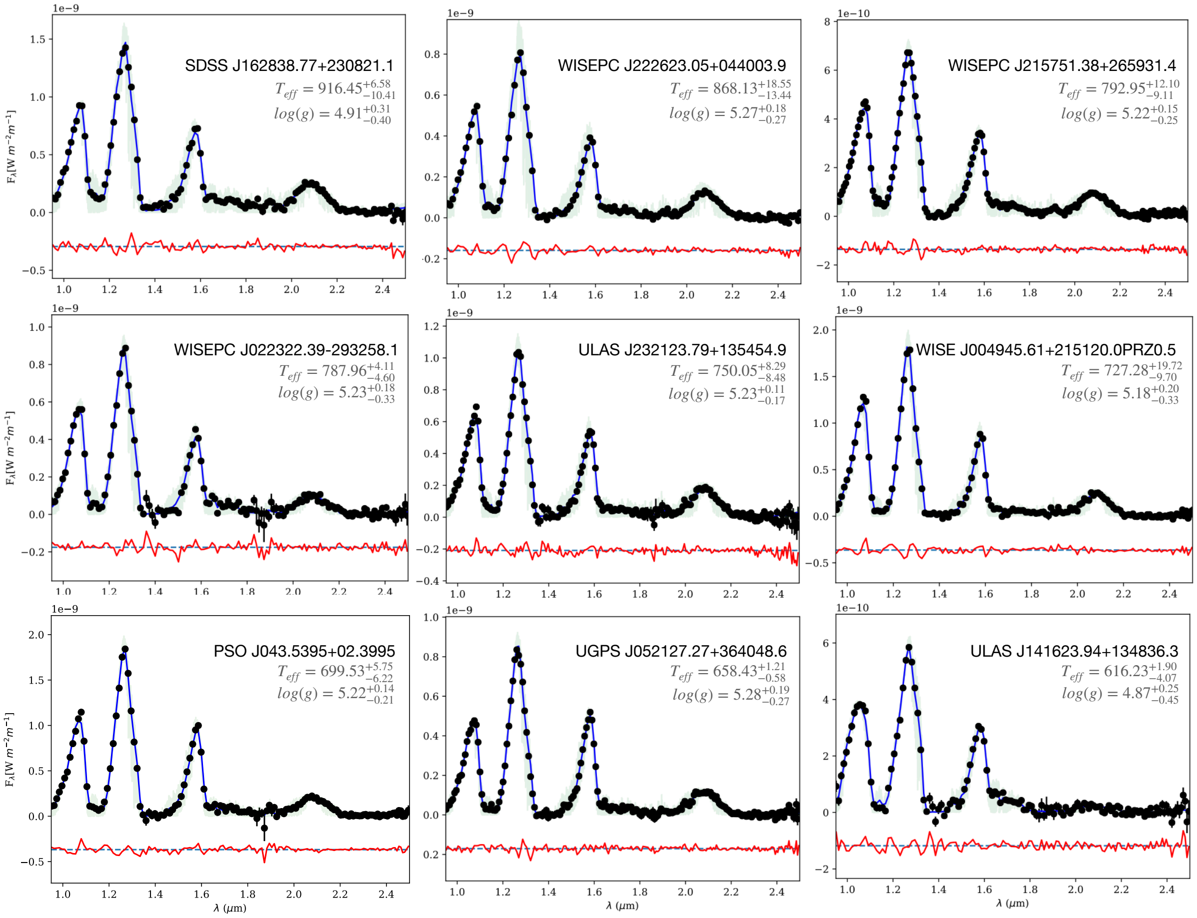

Figure 3.1: Best-fit plot for a sub-sample (arbitrarily selected to represent objects across the 950-500K range) of the 50 T dwarfs in this study. Black dots indicate "every other third" data points, the blue trace shows the best-fit retrieval model, and the residuals are shown in red. Also included in each panel are 1σ and 2σ confidence intervals (light green). The spectra are arranged according to their effective temperature (K).

(Burrows and Sharp, 1999).

Figure 3.3 shows molecular abundances of WFC3 Y and T dwarfs (Zalesky *et al.*, 2019), as well as the T dwarfs from this study. As shown in the figure, there are noticeable trends in the abundances of H_2O, CH_4, and NH_3. In general, the molecular abundances for early Y dwarfs are observed to be higher relative to molecular abundances of T dwarfs as expected. This is because cooler atmospheres are conducive environments for easily replenish-able large-scale molecular abundance. Hence, $T_{\rm eff}$

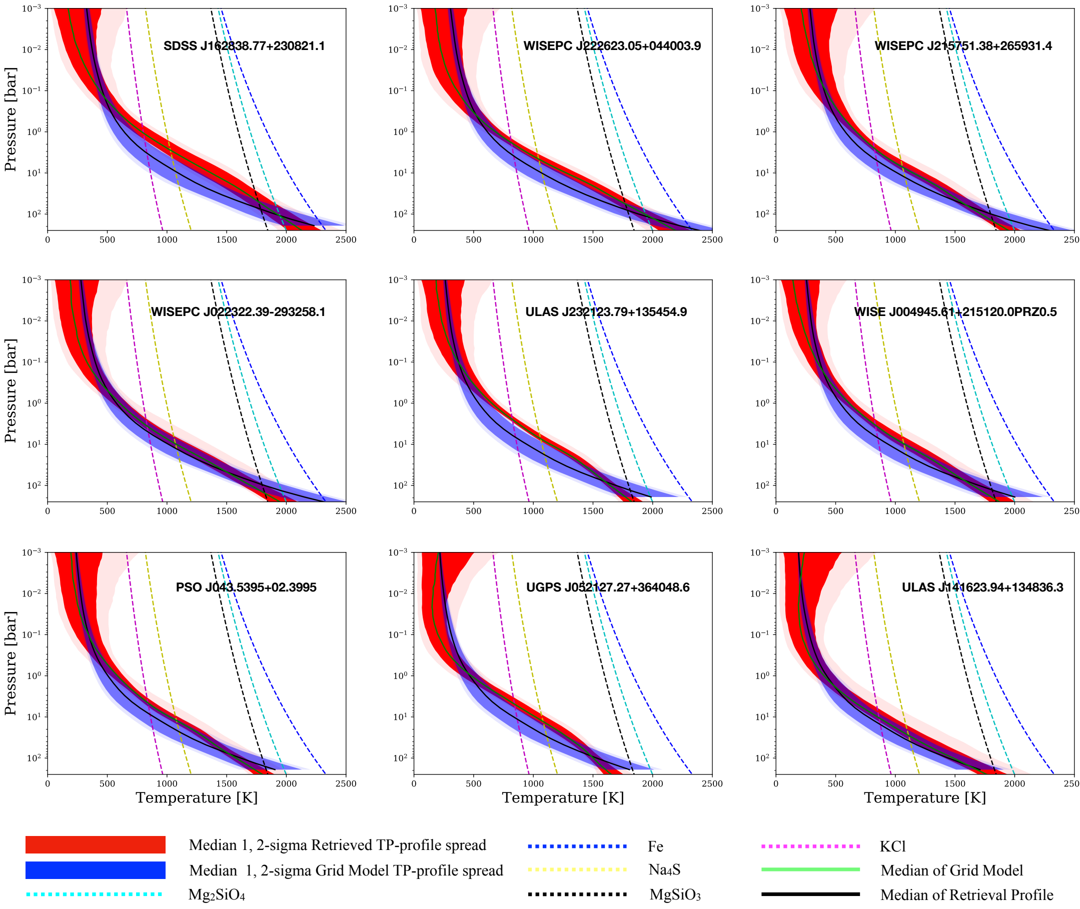

Figure 3.2: TP-profiles of representative T-dwarfs of my collection of 50 objects. The thermal profiles indicated here are of the retrieved objects (in red), and of grid models (in blue) that they closely compared to based on their similarities in a mix of T_{eff}, log(g), C/O, and metallicity parameters. For each of the thermals profiles, both 68% and 95% confidence intervals are shown. Equilibrium condensation curves of Mg_2SiO_4, Fe, $MaSiO_3$, Na_2S, and K are shown by the cyan, blue, black, yellow, and magenta dashed lines, respectively. The grid model of SDSS J162838.77+230821.1 is defined by T_{eff} = 900 K, log(g) = 5.0, [M/H] = 0.0, and C/O = 0.75, that of WISEPC J222623.05+044003.9 is defined by T_{eff} = 850 K, log(g) = 5.0, [M/H] = 0.0, and C/O = 0.80, that of WISEPC J215751.38+265931.4 is defined by T_{eff} = 800 K, log(g) = 5.0, [M/H] = 0.0, and C/O = 0.85, that of WISEPC J022322.39-293258.1 is defined by T_{eff} = 800 K, log(g), [M/H] = 0.0, and C/O = 0.5, that of ULAS J232123.79+135454.9 is defined by T_{eff} = 750 K, log(g) = 5.0, [M/H] = 0.0, C/O = 0.90, that of WISE J004945.61+215120.0PRZ0.5 is defined by T_{eff} = 750 K, log(g) = 5.0, [M/H] = 0.0, and C/O =0.90, that of PSO J043.5395+02.3995 are defined by T_{eff} = 700 K, log(g) = 5.0, [M/H] = 0.0, and C/O =0.90, that of UGPS J052127.27+364048.6 is defined by T_{eff} = 650 K, log(g) = 5.0, [M/H] = 0.5, C/O = 0.85, and that of ULAS J141623.94+134836.3 is defined by T_{eff} = 600 K, log(g) = 5.0, [M/H] = -0.50, and C/O = 0.50.

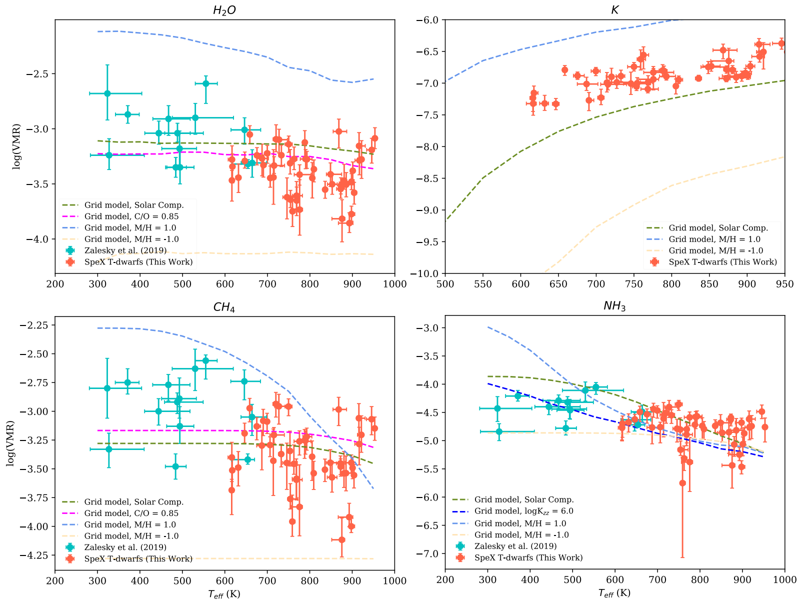

Figure 3.3: Molecular abundances (expressed as log of the VMRs) of H_2O, CH_4, NH_3, and K plotted against T_{eff} for T dwarfs from this study (color:tomato) and brown dwarfs from Zalesky *et al.* (2019). For K, objects from Zalesky *et al.* (2019) are not included because that work considered Na+K as one alkali species, whereas herein I am treating them as individual species. The four sub-plots show how the molecular and alkali abundances of each species varies with T_{eff}. All the modelled molecular abundance trends are defined by log(g) = 5.0 and solar composition (M/H = 0.0, C/O = 0.5), and I assume equilibrium chemistry unless otherwise specified. I observe that the overall trends of water, methane, and ammonia are consistent with solar chemistry curve models.

is a key factor affecting the concentration of molecular species in a brown dwarf's atmosphere.

To generate the predicted molecular abundance trends in Figure 3.3, I employ a sparse grid of 1D-radiative-convective-thermochemical (dis)equilibrium models over a range of gravities, effective temperatures, abundances (C/O and [M/H]), and eddy mixing (using the Zahnle and Marley (2014) prescription for the NH_3-N_2 and CO-CH_4 systems) using the ScCHIMERA framework described in Piskorz *et al.* (2018); Arcangeli *et al.* (2018); Mansfield *et al.* (2018); Kreidberg *et al.* (2018); Gharib-Nezhad and Line (2019); Zalesky *et al.* (2019); Colón *et al.* (2020); Beatty *et al.* (2020) under the standard rainout paradigm. Gas mixing ratios from the converged model atmospheres are then averaged over 30 - 1 bar for all models to compute an ”effective” abundance, on an equal footing to what the retrievals constrain. Inspecting Figure 3.3, I find that grid model solar composition is fairly consistent with water, ammonia, and methane abundance trends. Similar to the other three gases, the orientation of the emergent straight line that appears for K seems to be fairly consistent with the solar composition grid model, albeit that composition has a relatively higher VMR.

3.2.2 Metallicity and C/O Ratio

Unlike stars, brown dwarfs are generally known to have significant molecular abundances compared to individual elemental abundances due to their relatively low temperatures and internal pressures that are located at different layers of their atmospheres. In the NIR wavelength regime used in this study, some of the element ratios I determine are the C/O and [M/H] ratios. At such wavelengths, brown dwarfs contain vital identifiable oxygen and carbon-bearing molecules, as well as other molecular gas species. The C/O ratio is simply derived from C and O bearing gaseous species that are computed in the retrievals. For $T_{\rm eff}$ $\leq$1000 K, the most abundant source of carbon is methane, followed by both carbon monoxide and carbon dioxide. Oxygen is observed to be in high abundance in form of water vapour, and also in both carbon monoxide and carbon dioxide. Equation 3.1 summarizes how the C/O ratios for each of the objects were determined.

$$\frac{C}{O} = \frac{\Sigma C}{\Sigma O} \sim \frac{CH_4 + CO + CO_2}{H_2O + CO + 2CO_2} \tag{3.1}$$

For the collection of brown dwarfs, the range of C/O ratios is found to be from $0.41 \leq$ C/O ≤ 1.28 (see Table A.1 for reference). These ratios lie within reasonable extremes of the solar C/O ratio (0.55). This diversity in C/O ratios can be indicative of the different evolution patterns the various brown dwarfs may be undergoing. It also reveals fairly conspicuous hints about the nature of the environments in which they could have formed, in terms of whether or not they were formed amid other sub-stellar objects.

Taking a similar approach as in Zalesky *et al.* (2019), I determined the M/H ratio by summing up all species used in the retrieval process to determine the metallicity M and dividing by the molecular sum of hydrogen-bearing species used in the retrieval, as described in Equation 3.2.

$$[M/H] = log(\frac{(M/H)_{\mathrm{Tdwarf}}}{(M/H)_{\mathrm{solar}}}) \tag{3.2}$$

In Figure 3.5, I show how the metallicities of the retrieved objects compare with metallicities of a population of FGK stars (Hinkel *et al.*, 2014) as well as objects from Zalesky *et al.* (2019). In the figure, C/O ratios are plotted as a function of [M/H] ratio for the collection of retrieved brown dwarfs. Also plotted are the C/O ratios as a function of [Fe/H] for FGK spectral types. This crude comparison between stars and brown dwarfs reveals a noticeable metallicity discrepancy between the two groups of objects. Generally, the C/O values for stellar sources are smaller than the values for brown dwarfs at a given [Fe/H] or [M/H] value by ∼1-2σ. This suggests that the heavy element content in the stars is likely to be relatively higher compared to the heavy element content found late-T and Y dwarfs. The two populations of stars and brown dwarfs are relatively consistent with one another, which makes sense because they form under similar environments.

Figure 3.4 on the other hand shows a relationship between the N/C and C/O ratios. In the calculation of N/C, the only nitrogen-bearing gas that was considered was NH_3, while carbon-bearing gases were taken to be CH_4, CO, and CO_2, given the spectral wavelength range. In the figure I observe a characteristic clustering of the different late T-dwarfs within C/O and N/C ranges that are also observed in FGK stellar populations.

3.3 Other Derived Basic Physical Properties

Among the key diagnostic tools for understanding the evolution of brown dwarfs are effective temperature and surface gravity. Depending on the effective temperature of a brown dwarf, coupled with its size in terms radius and mass, its gravity can span the range of $3.5 \leq \log g \leq 5.5$ (Saumon and Marley, 2008). In principle, for a large

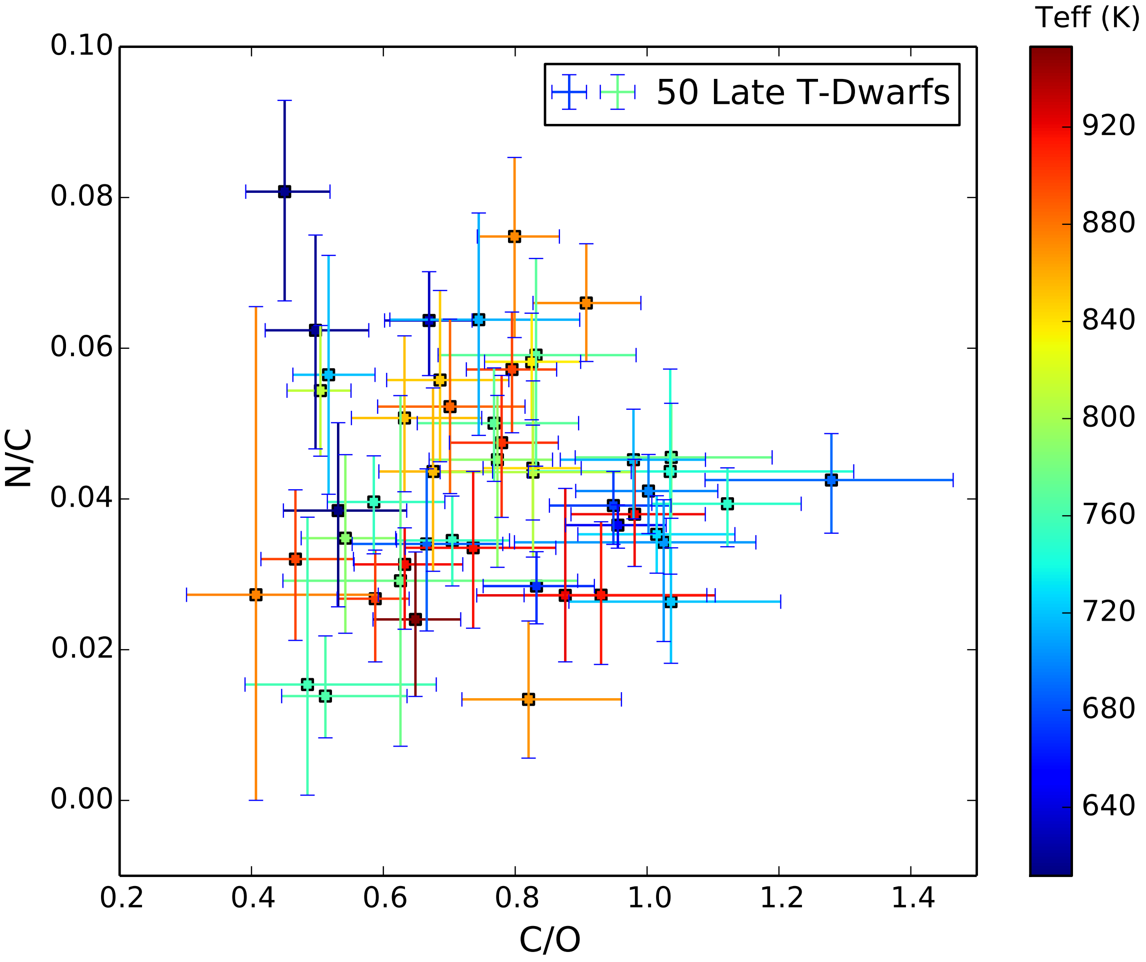

Figure 3.4: The N/O vs. C/O plot of the collection of 50 late T-dwarfs.

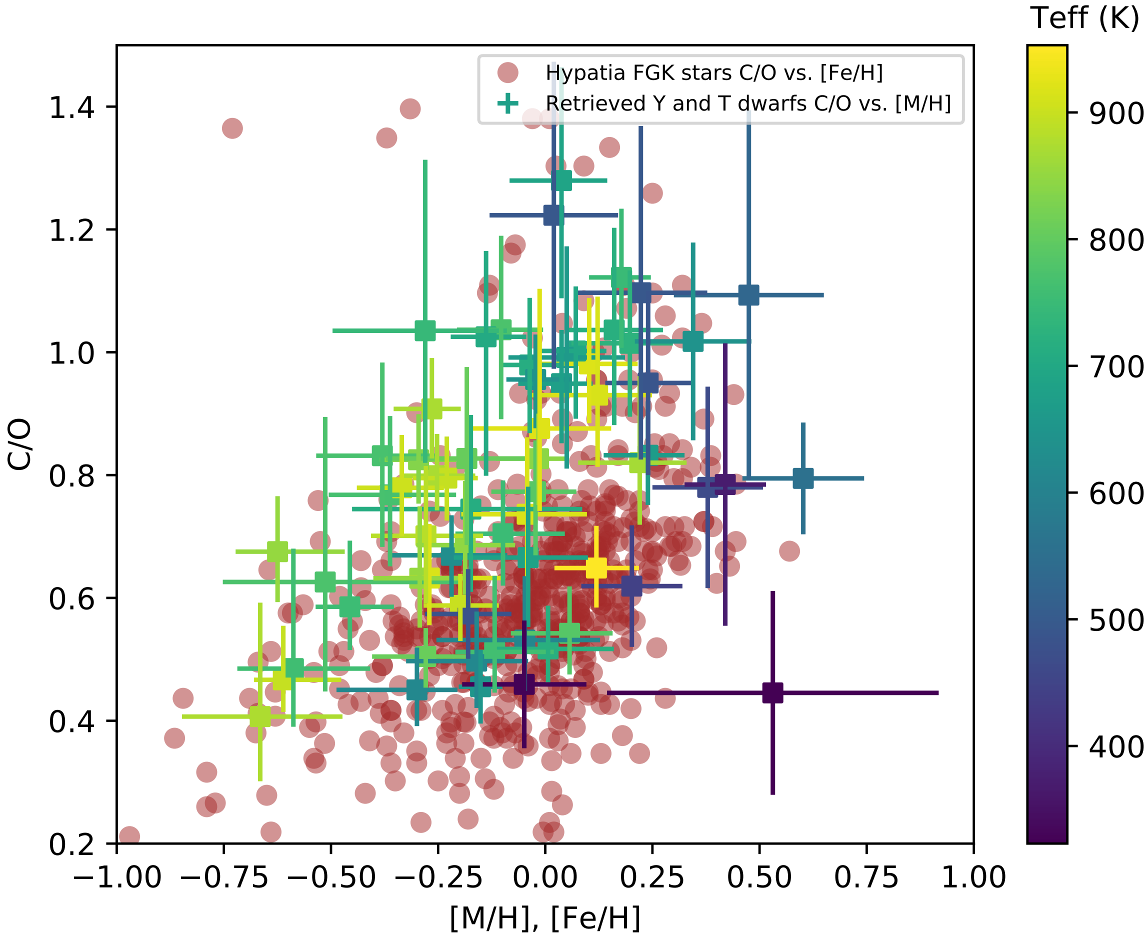

Figure 3.5: C/O vs. bulk metallicity of my Y and T dwarfs ensemble. The brown dwarfs are color-coded according to their effective temperatures. For comparison with field stars, I overplot the brown dwarfs (C/O vs. [M/H]) with Hypatia FGK stars(C/O vs. [Fe/H]) that are within comparable parallax distances (≤ 30 pc) to that of the brown dwarfs. I observe that my collection of brown dwarfs tends to have higher C/O ratios compared to those of the stars. Higher metalicities are observed typically for some Y dwarfs, as well as some early T dwarfs.

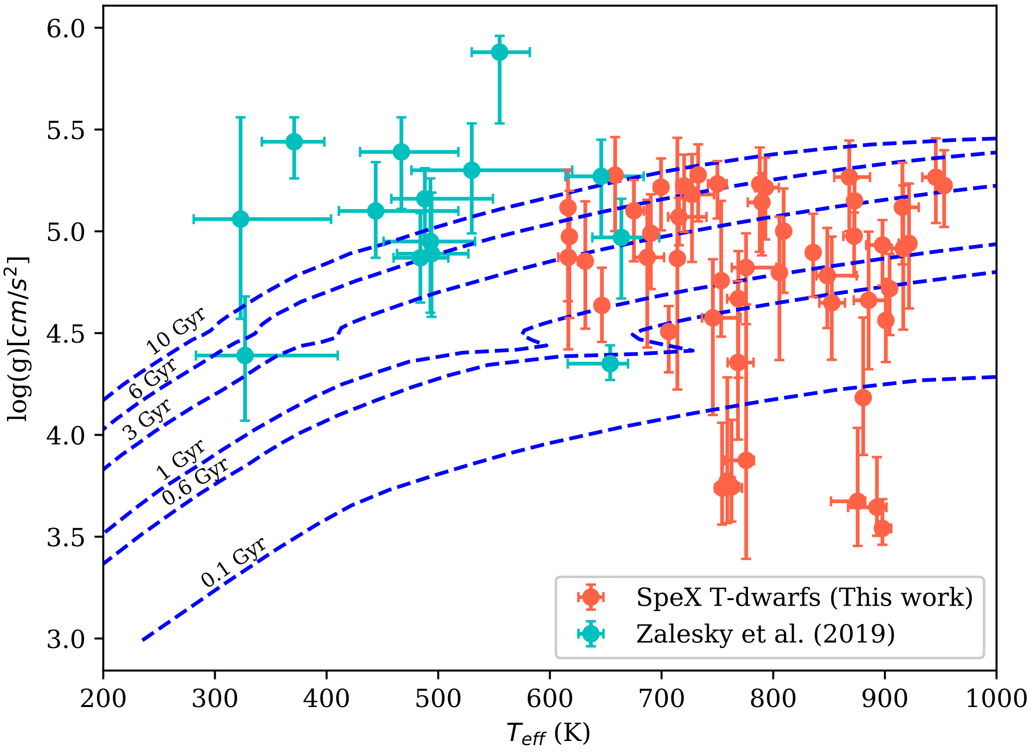

Figure 3.6: log g vs. $T_{\rm eff}$ for my collection of early Y dwarfs and late T dwarfs. Here I notice that I almost have a handful of T-dwarfs with low surface gravity values while Y- dwarfs tend to have higher gravity values. Based on evolutionary models from (Marley et al. (2020), in prep) (shown by blue dashed curves), T dwarfs having the lowest log g values would be relatively young (∼100 Myr) while Y dwarfs having the highest log g would be relatively old (∼12 Gyr). Most of the objects above the 10 Gyr curve are considered atypical although their high gravities can be justified by the logic that under-estimations of gravities that are done in grid models (Schneider *et al.*, 2015; Zalesky *et al.*, 2019).

enough collection of brown dwarfs, a plot of log(g) vs. $T_{\rm eff}$ should show a discernible overall distribution. Although relatively small, the distribution of objects in Figure 3.6 suggests there are a few brown dwarfs with $T_{\rm eff}$ >700 K and log(g) values of less than 4 cm s^{-2}. Brown dwarfs in this region are primarily thought to be younger relative to the ages of most T and Y dwarfs. The oddly low surface gravities are discussed further in 4.2.

3.4 Poor Retrievals

The initial collection of late T-dwarfs comprised of 56 objects. Out of this set, I produced satisfactory retrievals (in terms of constrained parameters) for the earlier highlighted 50 objects. However, the retrieval tool could not yield proper constraints for K and NH_3 for WISE J050003, WISE J062309, WISE J1809, and WISE J171104. For UGPS J072227, the retrieval could not get a good constrain on K only. Based on previous studies (Zalesky *et al.* (2019), Burrows *et al.* (2001)), the poor constraints on ammonia could stem from such processes such as vertical disequilibrium mixing that could be at plays within parts of the observed photospheres. Another reason could be that the retrieval framework is encountering a non-physical computations while exploring parameter space.

Chapter 4

DISCUSSION

4.1 Molecular Abundances and Condensation Curves

The altitude at which the condensation of molecules within the upper atmospheres of brown dwarfs occurs is largely contingent on the brown dwarf's $T_{\rm eff}$. In general, as illustrated in Figure 4.1, high $T_{\rm eff}$ objects tend to form condensates at higher altitudes than low $T_{\rm eff}$ do. Within a brown dwarf's atmosphere, elements such as C, O, and N can be sequestered depending on the condensation locations of the different condensates (Burrows *et al.*, 2001; Lodders, 2003). This could potentially be a attributing factor to the low metalicities of the the seven aforementioned T-dwarfs that are observed from their spectra.

The molecular abundances for water, ammonia, and methane present a recognizable trend that is consistent with some solar-based metallicity grid models. This discernible trend has been made possible by the use of a larger sample of brown dwarfs than has been used in previous studies. Due to their low effective temperatures, T dwarfs favor the formation of compound species that are in molecular form. The trend of water, ammonia, and methane abundances indicate that the hotter an object is, the lower its abundances of the aforementioned species. The converse is also evident from Figure 3.3. For K, however, the figure suggests that K abundances increase with increasing $T_{\rm eff}$in a fairly linear pattern.

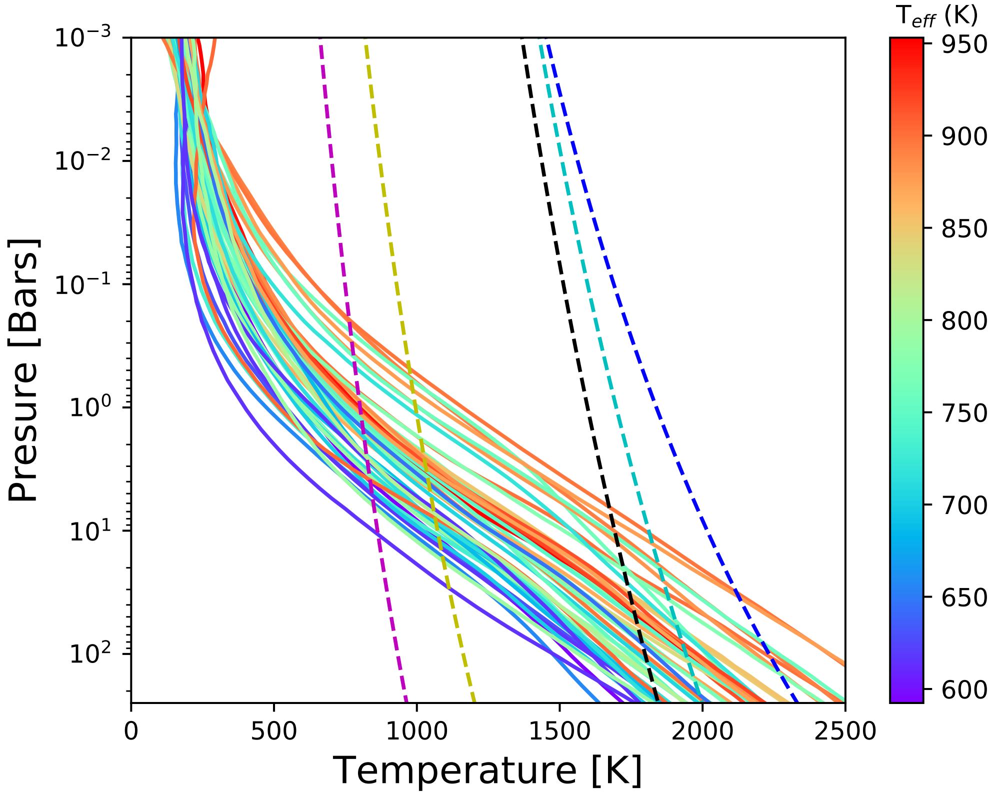

Figure 4.1: Summary of TP-profile medians (solid colored curves) of the 50 T dwarfs under study. The solid colored lines are arranged with respect to specific effective temperatures of the objects. The five dashed lines are representative of the condensation curves of Mg_2SiO_4 (cyan), $MgSiO_3$ (black), Fe (blue), KCl (pink), and Na_2S (yellow). On average, the TP-profile medians are arranged from coldest (lower left) to hottest (upper right), in agreement with TP-profile observations from radiative-convective equilibrium.

4.2 Metallicities and Surface Gravities of the Brown Dwarfs

The trend found in Figure 3.5 is consistent with that of similar results obtained in Parts II (Line *et al.* (2017)) and III (Zalesky *et al.* (2019)) of this series. The C/O ratios of the objects span 0.4-1.3 dex and the [M/H] ratios range from -0.7 to 0.65. This is typical of brown dwarfs (Madhusudhan *et al.*, 2016). Given that the overall chemical content of brown dwarfs undergoes insignificant alterations during their lifetime, the aforementioned ratios of the T dwarfs that I observe are arguably representative of the chemical nature of the molecular clouds from which they formed. Hence, by analyzing the ranges of the ratios, one can make inferences about the characteristic nature of the environments in which they form and evolve, and how diverse it is.

In Figure 3.6, seven T dwarfs appear to have lower surface gravity values compared to the rest of the objects. Among the seven objects is WISE J0325, which has the lowest log(g). Besides having a low log g, WISE J0325 is defined by comparatively low abundances of ammonia, methane, and water.

The other six objects with relatively low gravities are WISE J1254, PSO-J224, ROSS-458C, WISE-J1257, WISE-J1322, and WISE-J1959. Similar to WISE J0325, all the aforementioned T dwarfs, with the exception of ROSS-458C, register relatively low in both water and methane abundances. Furthermore, all seven of these T dwarfs have very low ammonia abundances. This observation of brown dwarfs exhibiting low gravities and molecular abundances is atypical because it is inconsistent with expectations that young brown dwarfs tend to showcase both low gravities and high metallicities (e.g., Helling and Casewell 2014). The younger a brown dwarf is, the more likely that it is characterized by high metallicity because the element abundances of interstellar molecular clouds from which brown dwarfs form increase overtime (Yuan *et al.* (2011)). Therefore, the generally older cooler brown dwarfs are characterised by lower element abundance content Helling and Casewell (2014). Moreover, the element abundance content of a brown dwarf is also influence by the chemical repository history of the environment in which it forms. Some brown dwarf formation regions can have insufficient elements while other can be replete with the elements (Cheng *et al.* (2012), Henry and Worthey (1999)).

The observed low metallicity of the young objects could stem from a myriad of causes such as the depth of the atmosphere to which I probe the brown dwarfs as well as cloud-thickness presence (Gagné *et al.*, 2014). The unusually low metallicities can perhaps be explained by the depletion of oxygen by silicate condensation processes in the objects that are younger than 0.1 Gyr. Oxygen accounts for a significant portion of metals within the atmospheres of the brown dwarfs. One striking feature of ROSS-458C is that it has a high [M/H] ratio, relative to that of the other six low gravity T dwarfs. This anomaly stems from a gravity-metallicity discrepancy effect.

4.3 Metallicity - Surface Gravity Relationship

To a large extent, the surface gravity of a brown dwarf goes hand in hand with its metallicity as referenced earlier. Both properties, together with mass, play a crucial collective role in defining the physical makeup of a brown dwarf. Low gravity, for instance, can be associated with low mass characteristics.

To test the credibility of the surface gravity values of the retrievals, I conducted a sanity check on the lowest gravity object (WISE 0325) and on the highest gravity objects (2MASS 0729) by varying their permitted priori gravity ranges. For WISE 0325, a retrieval with a full log (g) prior range of $0 \leq \log(g) \leq 6$ was compared to a retrieval done with a constrained log (g) prior range of $4.3 \leq \log(g) \leq 6$. The constrained log g prior for 2MASS 0729 was set to $0 \leq \log(g) \leq 4.3$ while the full range was maintained at $0 \leq \log(g) \leq 6$. In the limited cases, the gravity ranges were deliberately restricted to lower and higher gravity ranges to see how the retrieval system would behave. Figure 4.2 indicates that the retrievals favor higher gravities in the case of 2MASS 0729 and lower gravities in the case of WISE 0325. Alterations in gravity prior ranges also impact the convergence points of other species like water, ammonia, and methane, as is evident in Figure 4.2. This reinforces the evidence that gravity strongly correlates with these species. Hence parts of the spectra where gravity would be most evident would be regions where the absorption of these

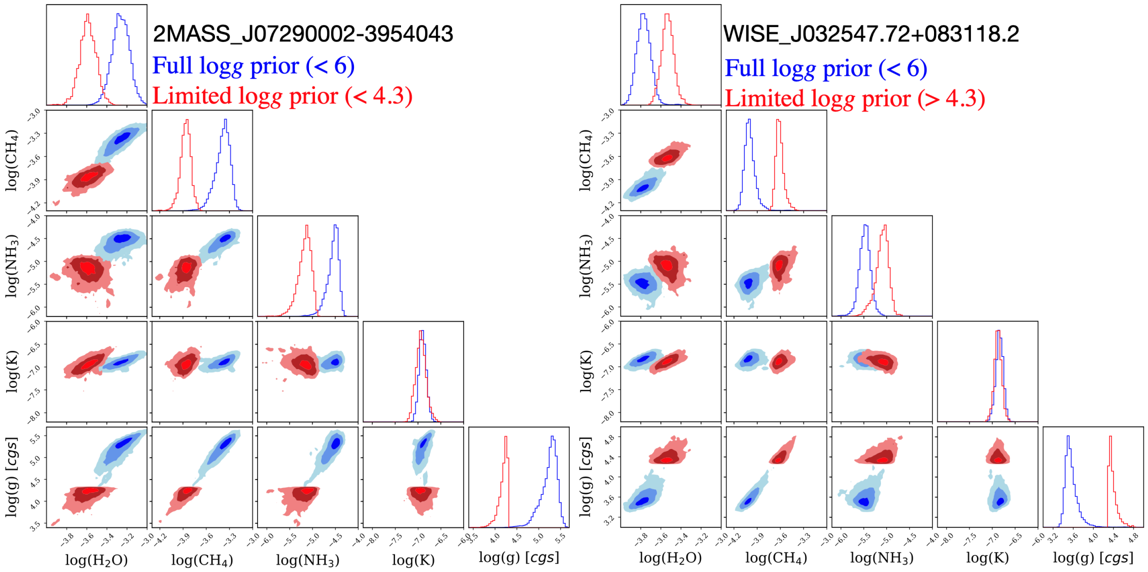

Figure 4.2: Corner plot posteriors of 2MASS-J072290002 (highest gravity object) and WISE-J032547.72 (lowest gravity object). This is based on a test of constraining priori ranges of gravity for the two objects. Gravity range restrictions affect gravity's correlation with the other gas species. Limited logg priors' results for surface gravity lean more toward full logg priors' results.

gases are most prominent. Potassium on the other hand appears to be insignificantly affected by changes in gravity. This is likely because potassium absorption features only affect a small portion of the spectrum between 0.95-2.5 μm, mostly in the $Y-$ and $J-$bandpasses. Changes in gravity priors also alters the thermal shapes of brown dwarfs, as is shown in Figure 4.3.

The T dwarfs vary in age depending on a combination of their effective temperature and gravities as illustrated in Figure 3.6. The vast majority of the objects (approximately 84%) are estimated to be between 100 Myr and 10 Gyr. One object is calculated to have an age that approaches that of the universe (i.e. above 10 Gyr), while the rest are young T dwarfs below 100 Myr. Relative to field stars, these young brown dwarfs have low surface gravities that are consistent with low masses and large radii. Overall, the calculated surface gravities of the brown dwarfs are well within my expectations. Over its lifetime, a brown dwarf is expected to cool down and con-

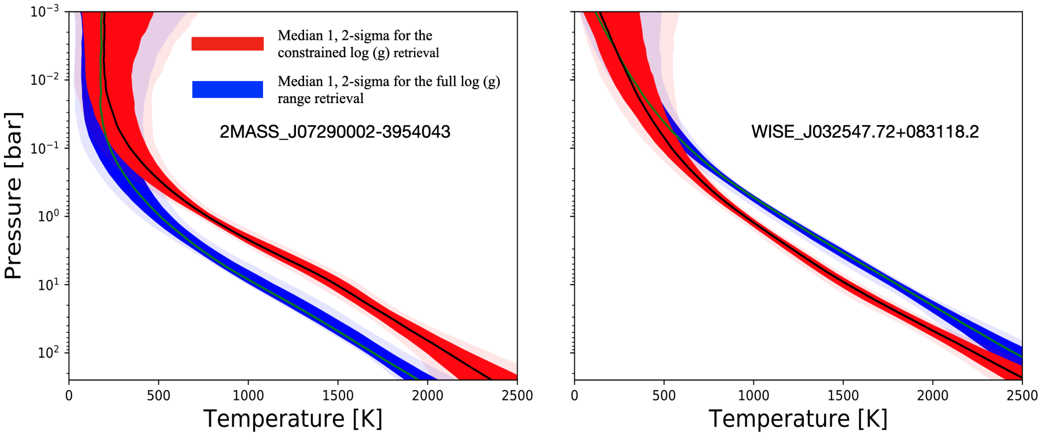

Figure 4.3: TP-profile comparisons of limited and full logg ranges retrievals for 2MASS-J07290002 and WISE-J032547. Restrictions in gravity ranges influence the shape of thermal profiles.

tract (Martin *et al.*, 2017). This inevitably leads to an increase in its surface gravity (Burrows and Sharp, 1999).

Chapter 5

SUMMARY AND CONCLUSIONS

This study of T dwarfs, combined with the results of Zalesky *et al.* (2019), provides insight into the dynamics that dictate the nature of brown dwarfs atmospheres at relatively low effective temperatures, in chemical content and overall evolution. Using my atmospheric retrieval tools, I have performed retrievals on a larger set of T-dwarfs using the same instrument routine than has previously been done (Line *et al.*, 2017; Zalesky *et al.*, 2019). This collection of brown dwarfs has allowed me to diagnose and explore fundamental composition trends and features that defines atmospheres of T-dwarfs and how they relate to properties of comparable stars and planets.

Among the conclusions that can be drawn from this analysis are:

1. In general, TP-profile structures of the T-dwarfs are consistent with TP-profiles created using the grid model approach. Probed photospheres reveal a cascading effect in the manner in which molecular compounds form with respect to altitude in terms of temperature since occurrences of condensation are more closely linked to temperature than they are to pressure (Burrows *et al.*, 2001). Simpler compounds such as H_2O form a higher altitudes than complex compounds like Fe do. The most evident condensates in the T-dwarfs are Na_2S and KCl. Condensates such as Mg_2SiO_4 and $MgSiO_3$ that form at deeper parts of the atmospheres highly depends on oxygen that is mostly sequestered from regions of photosphere that register higher concentrations of water. As is evident from figure 4.1, on average the shape of a T-dwarf is largely influenced by its effective temperatures. Other potential key drivers of the positioning of one TP-profile relative to another can be its mass, surface gravity level, as well as opacity

levels. Hence, as can be expected, TP-profiles vary among T-dwarfs based on a given T-dwarf's dominant spectral feature.

2. The analysis of a collection of brown dwarfs reveals some diagnostic composition trends for molecules species of water, ammonia, methane, and K. In general, the molecular abundances of each of these species from the Y-dwarfs (from Zalesky *et al.* 2019) and T-dwarfs form observable trends that are in line with modeled solar grid models. This makes solar elemental and molecular abundances suitable yardsticks for both categories of brown dwarfs. For my large set of Y and T-dwarfs (ranging from $\sim$ 350 K to $\sim$ 950 K), my results indicate that the range of H_2O spans from approximately -4.0 $\leq$ log(VMR) $\leq$ -2.5. Methane molecular abundances span from approximately -4.2 $\leq$ log(VMR) $\leq$ -2.5. The molecular abundances for ammonia and potassium species ranges from $\sim -6.0 \leq$ log(VMR) $\leq$ -4.0 and from $\sim -7.5 \leq$ log(VMR) $\leq$ -6.3, respectively. The trends for water, ammonia, and methane molecular abundances in figure 3.3 reveal that the more abundant these species are, the cooler the effective temperature of a brown dwarf is. Conversely, the trend observed for potassium hints that high abundance of K correlates with high effective temperature in the browns.

3. It was observed that the C/O ratios that define the T dwarfs in this study are largely super-solar. Some of the T dwarfs have been established to be carbon-rich. These observed high C/O ratio are also evident in some giant extra-solar planets such as WASP-12 (Madhusudhan *et al.*, 2011), which is an irradiated hot Jupiter. The overall noticeable trend is that the cooler a brown dwarf is, the more prone it is to exhibiting higher metallicities (see figure 3.5), also depending on gravity to a significant extent (Lodders and Fegley, 2002; Saumon

et al., 2000). Additionally, there is an observed consistency of FGK stars with the T and Y dwarfs, in terms of C/O ratio as function of metallicity.

4. As shown in figure 3.6, gravities of brown dwarf vary with effective temperature. On average, most Y-dwarfs appear to be relatively older than the majority of the T-dwarfs. In fact, some of the Y-dwarfs register ages of $\sim$ the age of the universe that seem fairly physically unrealistic. Generally, the objects are within plausible gravity-age evolution tracks. The reason behind such odd ages is yet to be explored. Out of the collection of objects shown in the aforementioned figure, seven T-dwarfs strikingly indicate low gravities. This could perhaps point out to the notion that the molecular clouds from which they formed were relatively small than that of most typical T-dwarfs. Differences in brown dwarf gravities can majorly be attributed to the nature of Y and J band-passes of spectra where it appears that surface gravity correlates with KI. Needless to say, the K and H bands of the infrared spectra also showcase changes to gravity, albeit small.

REFERENCES

Allard, F., P. H. Hauschildt, I. Baraffe and G. Chabrier, “Synthetic Spectra and Mass Determination of the Brown Dwarf GI 229B”, **465**, L123 (1996).

Arcangeli, J., J.-M. Désert, M. R. Line, J. L. Bean, V. Parmentier, K. B. Stevenson, L. Kreidberg, J. J. Fortney, M. Mansfield and A. P. Showman, “H^- Opacity and Water Dissociation in the Dayside Atmosphere of the Very Hot Gas Giant WASP-18b”, **855**, 2, L30 (2018).

Bate, M. R., I. A. Bonnell and V. Bromm, “The formation mechanism of brown dwarfs”, **332**, 3, L65–L68 (2002).

Beatty, T. G., I. Wong, T. Fetherolf, M. R. Line, A. Shporer, K. G. Stassun, G. R. Ricker, S. Seager, J. N. Winn, J. M. Jenkins, D. R. Louie, J. E. Schlieder, L. Sha, P. Tenenbaum and D. A. Yahalomi, “The TESS Phase Curve of KELT-1b Suggests a High Dayside Albedo”, arXiv e-prints p. arXiv:2006.10292 (2020).

Becklin, E. E. and B. Zuckerman, “A low-temperature companion to a white dwarf star”, **336**, 6200, 656–658 (1988).

Best, W. M. J., M. C. Liu, E. A. Magnier and T. J. Dupuy, “The Hawaii Infrared Parallax Program. IV. A Comprehensive Parallax Survey of L0-T8 Dwarfs with UKIRT”, **159**, 6, 257 (2020).

Best, W. M. J., E. A. Magnier, M. C. Liu, K. M. Aller, Z. Zhang, W. S. Burgett, K. C. Chambers, P. Draper, H. Flewelling, N. Kaiser, R. P. Kudritzki, N. Metcalfe, J. L. Tonry, R. J. Wainscoat and C. Waters, “Photometry and Proper Motions of M, L, and T Dwarfs from the Pan-STARRS1 3π Survey”, **234**, 1, 1 (2018).

Burgasser, A. J., “The SpeX Prism Library: 1000+ low-resolution, near-infrared spectra of ultracool M, L, T and Y dwarfs”, in “Astronomical Society of India Conference Series”, vol. 11 of *Astronomical Society of India Conference Series*, pp. 7–16 (2014).

Burrows, A., W. B. Hubbard, J. I. Lunine and J. Liebert, “The theory of brown dwarfs and extrasolar giant planets”, Reviews of Modern Physics **73**, 3, 719–765 (2001).

Burrows, A. and C. M. Sharp, “Chemical Equilibrium Abundances in Brown Dwarf and Extrasolar Giant Planet Atmospheres”, **512**, 2, 843–863 (1999).

Canty, J. I., P. W. Lucas, S. N. Yurchenko, J. Tennyson, S. K. Leggett, C. G. Tinney, H. R. A. Jones, B. Burningham, D. J. Pinfield and R. L. Smart, “Methane and ammonia in the near-infrared spectra of late-T dwarfs”, **450**, 1, 454–480 (2015).

Chabrier, G., I. Baraffe, F. Selsis, T. S. Barman, P. Hennebelle and Y. Alibert, “Gaseous Planets, Protostars, and Young Brown Dwarfs: Birth and Fate”, in “Protostars and Planets V”, edited by B. Reipurth, D. Jewitt and K. Keil, p. 623 (2007).

Cheng, J. Y., C. M. Rockosi, H. L. Morrison, R. A. Schönrich, Y. S. Lee, T. C. Beers, D. Bizyaev, K. Pan and D. P. Schneider, "Metallicity Gradients in the Milky Way Disk as Observed by the SEGUE Survey", **746**, 2, 149 (2012).

Colón, K. D., L. Kreidberg, M. Line, L. Welbanks, N. Madhusudhan, T. Beatty, P. Tamburo, K. B. Stevenson, A. Mandell, J. E. Rodriguez, T. Barclay, E. D. Lopez, K. G. Stassun, D. Angerhausen, J. J. Fortney, D. J. James, J. Pepper, J. P. Ahlers, P. Plavchan, S. Awiphan, C. Kotnik, K. K. McLeod, G. Murawski, H. Chotani, D. LeBrun, W. Matzko, D. Rea, M. Vidaurri, S. Webster, J. K. Williams, L. Sheraden Cox, N. Tan and E. A. Gilbert, "An Unusual Transmission Spectrum for the Sub-Saturn KELT-11b Suggestive of a Sub-Solar Water Abundance", arXiv e-prints p. arXiv:2005.05153 (2020).

Czekala, I., S. M. Andrews, K. S. Mandel, D. W. Hogg and G. M. Green, "Starfish: Robust spectroscopic inference tools", (2015).

Dupuy, T. J. and M. C. Liu, "The Hawaii Infrared Parallax Program. I. Ultracool Binaries and the L/T Transition", **201**, 2, 19 (2012).

Fletcher, L. N., P. G. J. Irwin, N. A. Teanby, G. S. Orton, P. D. Parrish, R. de Kok, C. Howett, S. B. Calcutt, N. Bowles and F. W. Taylor, "Characterising Saturn's vertical temperature structure from Cassini/CIRS", **189**, 2, 457–478 (2007).

Foreman-Mackey, D., D. W. Hogg, D. Lang and J. Goodman, "emcee: The MCMC Hammer", **125**, 925, 306 (2013).

Gagné, J., D. Lafrenière, R. Doyon, É. Artigau, L. Malo, J. Robert and D. Nadeau, "SIMP J2154-1055: A New Low-gravity L4β Brown Dwarf Candidate Member of the Argus Association", **792**, 1, L17 (2014).

Gharib-Nezhad, E. and M. R. Line, "The Influence of H_2O Pressure Broadening in High-metallicity Exoplanet Atmospheres", **872**, 1, 27 (2019).

Greathouse, T. K., M. Richter, J. Lacy, J. Moses, G. Orton, T. Encrenaz, H. B. Hammel and D. Jaffe, "A spatially resolved high spectral resolution study of Neptune's stratosphere", **214**, 2, 606–621 (2011).

Hayashi, C. and T. Nakano, "Evolution of Stars of Small Masses in the Pre-Main-Sequence Stages", Progress of Theoretical Physics **30**, 4, 460–474 (1963).

Helling, C. and S. Casewell, "Atmospheres of brown dwarfs", **22**, 80 (2014).

Hennebelle, P., "Formation of Low-Mass Stars and Brown Dwarfs", in "EAS Publications Series", edited by C. Reylé, C. Charbonnel and M. Schultheis, vol. 57 of *EAS Publications Series*, pp. 91–127 (2012).

Henry, R. B. C. and G. Worthey, "The Distribution of Heavy Elements in Spiral and Elliptical Galaxies", **111**, 762, 919–945 (1999).

Hinkel, N. R., F. X. Timmes, P. A. Young, M. D. Pagano and M. C. Turnbull, "Stellar Abundances in the Solar Neighborhood: The Hypatia Catalog", **148**, 3, 54 (2014).

Irwin, P. G. J., N. A. Teanby, R. de Kok, L. N. Fletcher, C. J. A. Howett, C. C. C. Tsang, C. F. Wilson, S. B. Calcutt, C. A. Nixon and P. D. Parrish, “The NEMESIS planetary atmosphere radiative transfer and retrieval tool”, **109**, 1136–1150 (2008).

Kirkpatrick, J. D., “New Spectral Types L and T”, **43**, 1, 195–245 (2005).

Kreidberg, L., M. R. Line, D. Thorngren, C. V. Morley and K. B. Stevenson, “Water, High-altitude Condensates, and Possible Methane Depletion in the Atmosphere of the Warm Super-Neptune WASP-107b”, **858**, 1, L6 (2018).

Krumholz, M. R., C. F. McKee and R. I. Klein, “The formation of stars by gravitational collapse rather than competitive accretion”, **438**, 7066, 332–334 (2005).

Line, M. R., J. J. Fortney, M. S. Marley and S. Sorahana, “A Data-driven Approach for Retrieving Temperatures and Abundances in Brown Dwarf Atmospheres”, **793**, 1, 33 (2014).

Line, M. R., M. S. Marley, M. C. Liu, B. Burningham, C. V. Morley, N. R. Hinkel, J. Teske, J. J. Fortney, R. Freedman and R. Lupu, “Uniform Atmospheric Retrieval Analysis of Ultracool Dwarfs. II. Properties of 11 T dwarfs”, **848**, 2, 83 (2017).

Line, M. R., J. Teske, B. Burningham, J. J. Fortney and M. S. Marley, “Uniform Atmospheric Retrieval Analysis of Ultracool Dwarfs. I. Characterizing Benchmarks, Gl 570D and HD 3651B”, **807**, 2, 183 (2015).

Lodders, K., “Solar System Abundances and Condensation Temperatures of the Elements”, **591**, 2, 1220–1247 (2003).

Lodders, K. and B. Fegley, “Atmospheric Chemistry in Giant Planets, Brown Dwarfs, and Low-Mass Dwarf Stars. I. Carbon, Nitrogen, and Oxygen”, **155**, 2, 393–424 (2002).

Madhusudhan, N., “Exoplanetary Atmospheres: Thermal Inversions and Self-consistent Models”, in “Radiative Signatures from the Cosmos”, edited by K. Werner, C. Stehle, T. Rauch and T. Lanz, vol. 519 of *Astronomical Society of the Pacific Conference Series*, p. 129 (2019).

Madhusudhan, N., D. Apai and S. Gandhi, “Atmospheric Compositions of Three Brown Dwarfs and Implications for their Formation Conditions”, arXiv e-prints p. arXiv:1612.03174 (2016).

Madhusudhan, N., A. Burrows and T. Currie, “Model Atmospheres for Massive Gas Giants with Thick Clouds: Application to the HR 8799 Planets and Predictions for Future Detections”, **737**, 1, 34 (2011).

Mansfield, M., J. L. Bean, M. R. Line, V. Parmentier, L. Kreidberg, J.-M. Désert, J. J. Fortney, K. B. Stevenson, J. Arcangeli and D. Dragomir, “An HST/WFC3 Thermal Emission Spectrum of the Hot Jupiter HAT-P-7b”, **156**, 1, 10 (2018).

Marley, M. S. and T. D. Robinson, “On the Cool Side: Modeling the Atmospheres of Brown Dwarfs and Giant Planets”, **53**, 279–323 (2015).

Marley, M. S., D. Saumon, T. Guillot, R. S. Freedman, W. B. Hubbard, A. Burrows and J. I. Lunine, “Atmospheric, Evolutionary, and Spectral Models of the Brown Dwarf Gliese 229 B”, Science **272**, 5270, 1919–1921 (1996).

Martin, E. C., G. N. Mace, I. S. McLean, S. E. Logsdon, E. L. Rice, J. D. Kirkpatrick, A. J. Burgasser, M. R. McGovern and L. Prato, “Surface Gravities for 228 M, L, and T Dwarfs in the NIRSPEC Brown Dwarf Spectroscopic Survey”, **838**, 1, 73 (2017).

Oppenheimer, B. R., S. R. Kulkarni, K. Matthews and T. Nakajima, “Infrared Spectrum of the Cool Brown Dwarf Gl 229B”, Science **270**, 5241, 1478–1479 (1995).

Patience, J., R. R. King, R. J. De Rosa, A. Vigan, S. Witte, E. Rice, C. Helling and P. Hauschildt, “Spectroscopy across the brown dwarf/planetary mass boundary. I. Near-infrared JHK spectra”, **540**, A85 (2012).

Piskorz, D., C. Buzard, M. R. Line, H. A. Knutson, B. Benneke, N. R. Crockett, A. C. Lockwood, G. A. Blake, T. S. Barman, C. F. Bender, D. Deming and J. A. Johnson, “Ground- and space-based detection of the thermal emission spectrum of the transiting hot jupiter KELT-2ab”, The Astronomical Journal **156**, 3, 133, URL

Rayner, J. T., D. W. Toomey, P. M. Onaka, A. J. Denault, W. E. Stahlberger, W. D. Vacca, M. C. Cushing and S. Wang, “SpeX: A Medium-Resolution 0.8-5.5 Micron Spectrograph and Imager for the NASA Infrared Telescope Facility”, **115**, 805, 362–382 (2003).

Rebolo, R., M. R. Zapatero Osorio and E. L. Martín, “Discovery of a brown dwarf in the Pleiades star cluster”, **377**, 6545, 129–131 (1995).

Saumon, D., T. R. Geballe, S. K. Leggett, M. S. Marley, R. S. Freedman, K. Lodders, J. Fegley, B. and S. K. Sengupta, “Molecular Abundances in the Atmosphere of the T Dwarf GL 229B”, **541**, 1, 374–389 (2000).

Saumon, D. and M. S. Marley, “The Evolution of L and T Dwarfs in Color-Magnitude Diagrams”, **689**, 2, 1327–1344 (2008).

Saumon, D., M. S. Marley, M. C. Cushing, S. K. Leggett, T. L. Roellig, K. Lodders and R. S. Freedman, “Ammonia as a Tracer of Chemical Equilibrium in the T7.5 Dwarf Gliese 570D”, **647**, 1, 552–557 (2006).

Schneider, A. C., M. C. Cushing, J. D. Kirkpatrick, C. R. Gelino, G. N. Mace, E. L. Wright, P. R. Eisenhardt, M. F. Skrutskie, R. L. Griffith and K. A. Marsh, “Hubble Space Telescope Spectroscopy of Brown Dwarfs Discovered with the Wide-field Infrared Survey Explorer”, **804**, 2, 92 (2015).

Shu, F. H., “Self-similar collapse of isothermal spheres and star formation.”, **214**, 488–497 (1977).

Uehara, H. and S.-i. Inutsuka, “Does Deuterium Enable the Formation of Primordial Brown Dwarfs?”, **531**, 2, L91–L94 (2000).

Whitworth, A., M. R. Bate, Å. Nordlund, B. Reipurth and H. Zinnecker, "The Formation of Brown Dwarfs: Theory", in "Protostars and Planets V", edited by B. Reipurth, D. Jewitt and K. Keil, p. 459 (2007).

Whitworth, A. P. and D. Stamatellos, "The minimum mass for star formation, and the origin of binary brown dwarfs", Astronomy Astrophysics **458**, 3, 817–829, URL `http://dx.doi.org/10.1051/0004-6361:20065806` (2006).

Yuan, T. T., L. J. Kewley, A. M. Swinbank, J. Richard and R. C. Livermore, "Metallicity Gradient of a Lensed Face-on Spiral Galaxy at Redshift 1.49", **732**, 1, L14 (2011).

Zahnle, K. J. and M. S. Marley, "Methane, Carbon Monoxide, and Ammonia in Brown Dwarfs and Self-Luminous Giant Planets", **797**, 1, 41 (2014).

Zalesky, J. A., M. R. Line, A. C. Schneider and J. Patience, "A Uniform Retrieval Analysis of Ultra-cool Dwarfs. III. Properties of Y Dwarfs", **877**, 1, 24 (2019).

APPENDIX A

ATMOSPHERIC ABUNDANCES AND DERIVED PARAMETERS

Object	$T_{\rm eff}$ [K]	log(g) [cgs]	R [R_J]	H_2O [VMR]	CH_4 [VMR]	NH_3 [VMR]	K [VMR]	[M/H]	C/O
WISE-PCJ0458	$616.50^{+4.15}_{-9.05}$	$4.87^{+0.25}_{-0.45}$	$1.15^{+0.14}_{-0.13}$	$-3.28^{+0.12}_{-0.19}$	$-3.40^{+0.13}_{-0.21}$	$-4.77^{+0.16}_{-0.23}$	$-7.32^{+0.14}_{-0.18}$	$-0.05^{+0.18}_{-0.21}$	$0.53^{+0.10}_{-0.08}$
ULAS-J1416	$616.23^{+1.90}_{-4.07}$	$5.12^{+0.19}_{-0.46}$	$0.93^{+0.07}_{-0.06}$	$-3.47^{+0.09}_{-0.19}$	$-3.69^{+0.09}_{-0.21}$	$-4.76^{+0.11}_{-0.23}$	$-7.23^{+0.10}_{-0.21}$	$-0.38^{+0.09}_{-0.19}$	$0.45^{+0.07}_{-0.06}$
2MASS-J1114	$617.46^{+5.43}_{-2.78}$	$4.97^{+0.22}_{-0.40}$	$1.01^{+0.11}_{-0.11}$	$-3.34^{+0.11}_{-0.15}$	$-3.51^{+0.11}_{-0.19}$	$-4.70^{+0.14}_{-0.24}$	$-7.16^{+0.11}_{-0.15}$	$-0.24^{+0.12}_{-0.17}$	$0.50^{+0.08}_{-0.08}$
2MASS-J0939	$631.72^{+5.13}_{-6.67}$	$4.85^{+0.29}_{-0.33}$	$1.01^{+0.06}_{-0.06}$	$-3.44^{+0.12}_{-0.13}$	$-3.49^{+0.14}_{-0.16}$	$-4.68^{+0.15}_{-0.17}$	$-7.32^{+0.13}_{-0.11}$	$-0.29^{+0.13}_{-0.15}$	$0.67^{+0.07}_{-0.07}$
WISE-PAJ1741	$646.58^{+4.26}_{-4.58}$	$4.64^{+0.18}_{-0.18}$	$0.84^{+0.03}_{-0.04}$	$-3.29^{+0.08}_{-0.06}$	$-3.19^{+0.09}_{-0.08}$	$-4.62^{+0.09}_{-0.10}$	$-7.33^{+0.09}_{-0.09}$	$-0.08^{+0.08}_{-0.07}$	$0.95^{+0.07}_{-0.08}$
UGPS-J0521	$658.43^{+1.21}_{-0.58}$	$5.28^{+0.19}_{-0.27}$	$0.74^{+0.04}_{-0.05}$	$-3.05^{+0.08}_{-0.08}$	$-2.97^{+0.09}_{-0.12}$	$-4.49^{+0.10}_{-0.17}$	$-6.79^{+0.07}_{-0.09}$	$0.24^{+0.09}_{-0.10}$	$0.83^{+0.09}_{-0.08}$
2MASS-J0415	$675.24^{+8.95}_{-5.38}$	$5.10^{+0.15}_{-0.25}$	$0.94^{+0.06}_{-0.06}$	$-3.24^{+0.07}_{-0.09}$	$-3.13^{+0.08}_{-0.12}$	$-4.53^{+0.09}_{-0.16}$	$-6.88^{+0.06}_{-0.06}$	$-0.02^{+0.07}_{-0.10}$	$0.96^{+0.09}_{-0.10}$
WISE-J1653	$687.22^{+15.06}_{-12.25}$	$4.87^{+0.28}_{-0.44}$	$1.03^{+0.12}_{-0.13}$	$-3.27^{+0.13}_{-0.16}$	$-3.30^{+0.13}_{-0.21}$	$-4.77^{+0.19}_{-0.29}$	$-7.01^{+0.11}_{-0.10}$	$-0.11^{+0.14}_{-0.19}$	$0.66^{+0.12}_{-0.11}$
ULAS -J1029	$690.39^{+6.46}_{-3.34}$	$4.99^{+0.19}_{-0.27}$	$1.04^{+0.09}_{-0.09}$	$-3.33^{+0.09}_{-0.11}$	$-3.08^{+0.10}_{-0.13}$	$-4.44^{+0.10}_{-0.15}$	$-7.27^{+0.12}_{-0.16}$	$-0.01^{+0.11}_{-0.12}$	$1.28^{+0.18}_{-0.19}$
PSO-J043	$699.53^{+5.75}_{-6.22}$	$5.22^{+0.14}_{-0.21}$	$0.84^{+0.06}_{-0.06}$	$-3.22^{+0.07}_{-0.09}$	$-3.09^{+0.07}_{-0.10}$	$-4.47^{+0.08}_{-0.14}$	$-6.81^{+0.06}_{-0.07}$	$0.02^{+0.07}_{-0.10}$	$1.00^{+0.10}_{-0.11}$
WISE-J1813	$706.42^{+4.04}_{-4.45}$	$4.51^{+0.13}_{-0.20}$	$2.04^{+0.19}_{-0.35}$	$-3.45^{+0.11}_{-0.08}$	$-3.29^{+0.07}_{-0.10}$	$-4.76^{+0.09}_{-0.27}$	$-7.23^{+0.13}_{-0.11}$	$-0.19^{+0.09}_{-0.08}$	$1.02^{+0.14}_{-0.23}$
WISE-J2319	$714.16^{+5.82}_{-2.84}$	$4.87^{+0.59}_{-0.64}$	$0.62^{+0.09}_{-0.07}$	$-3.44^{+0.25}_{-0.25}$	$-3.43^{+0.28}_{-0.30}$	$-4.61^{+0.29}_{-0.32}$	$-6.99^{+0.16}_{-0.15}$	$-0.24^{+0.26}_{-0.28}$	$0.74^{+0.15}_{-0.13}$
HD3651B	$715.57^{+24.68}_{-9.65}$	$5.07^{+0.09}_{-0.14}$	$1.17^{+0.10}_{-0.10}$	$-3.33^{+0.08}_{-0.07}$	$-3.21^{+0.07}_{-0.07}$	$-4.54^{+0.07}_{-0.09}$	$-7.02^{+0.07}_{-0.09}$	$-0.04^{+0.08}_{-0.07}$	$0.98^{+0.11}_{-0.11}$
2MASS-J0729	$719.36^{+6.39}_{-5.10}$	$5.28^{+0.15}_{-0.23}$	$0.82^{+0.10}_{-0.09}$	$-3.24^{+0.09}_{-0.10}$	$-3.37^{+0.09}_{-0.11}$	$-4.55^{+0.10}_{-0.15}$	$-6.89^{+0.09}_{-0.09}$	$0.01^{+0.15}_{-0.13}$	$0.52^{+0.05}_{-0.07}$
WISE-J2255	$720.23^{+3.48}_{-7.03}$	$5.22^{+0.15}_{-0.23}$	$0.89^{+0.11}_{-0.10}$	$-3.09^{+0.12}_{-0.11}$	$-2.94^{+0.10}_{-0.11}$	$-4.51^{+0.11}_{-0.18}$	$-6.90^{+0.13}_{-0.12}$	$0.16^{+0.11}_{-0.11}$	$1.04^{+0.17}_{-0.15}$
WISE-J0049	$727.28^{+19.72}_{-9.70}$	$5.18^{+0.20}_{-0.33}$	$0.81^{+0.07}_{-0.07}$	$-3.09^{+0.09}_{-0.12}$	$-2.96^{+0.15}_{-0.10}$	$-4.40^{+0.12}_{-0.19}$	$-6.99^{+0.09}_{-0.10}$	$0.14^{+0.10}_{-0.14}$	$1.01^{+0.12}_{-0.12}$
WISE-J1039	$745.93^{+24.79}_{-9.72}$	$4.58^{+0.29}_{-0.48}$	$1.46^{+0.26}_{-0.23}$	$-3.62^{+0.18}_{-0.20}$	$-3.45^{+0.17}_{-0.23}$	$-4.79^{+0.17}_{-0.24}$	$-7.01^{+0.18}_{-0.17}$	$-0.33^{+0.19}_{-0.22}$	$1.03^{+0.28}_{-0.21}$
ULAS-J2321	$750.05^{+8.29}_{-8.48}$	$5.23^{+0.11}_{-0.17}$	$0.90^{+0.06}_{-0.07}$	$-3.14^{+0.07}_{-0.07}$	$-2.96^{+0.07}_{-0.08}$	$-4.36^{+0.07}_{-0.11}$	$-6.74^{+0.07}_{-0.07}$	$0.13^{+0.07}_{-0.08}$	$1.12^{+0.11}_{-0.11}$
WISE-J2000	$753.40^{+3.29}_{-5.34}$	$4.76^{+0.39}_{-0.27}$	$0.90^{+0.06}_{-0.05}$	$-3.31^{+0.12}_{-0.10}$	$-3.34^{+0.17}_{-0.13}$	$-4.80^{+0.21}_{-0.17}$	$-7.05^{+0.07}_{-0.06}$	$-0.17^{+0.15}_{-0.11}$	$0.70^{+0.09}_{-0.08}$
WISE-PAJ1959	$754.21^{+17.80}_{-6.23}$	$3.74^{+0.32}_{-0.18}$	$0.91^{+0.07}_{-0.06}$	$-3.64^{+0.08}_{-0.07}$	$-3.76^{+0.07}_{-0.13}$	$-5.16^{+0.15}_{-0.10}$	$-7.00^{+0.09}_{-0.09}$	$-0.53^{+0.11}_{-0.08}$	$0.58^{+0.11}_{-0.07}$
WISE-J1257	$758.90^{+6.54}_{-4.72}$	$3.77^{+0.51}_{-0.21}$	$0.89^{+0.18}_{-0.09}$	$-3.75^{+0.14}_{-0.14}$	$-3.96^{+0.23}_{-0.13}$	$-5.75^{+0.46}_{-1.32}$	$-6.62^{+0.15}_{-0.17}$	$-0.67^{+0.19}_{-0.13}$	$0.48^{+0.19}_{-0.09}$
ROSS458C	$762.64^{+6.85}_{-1.81}$	$3.74^{+0.33}_{-0.17}$	$0.87^{+0.09}_{-0.05}$	$-3.27^{+0.11}_{-0.10}$	$-3.46^{+0.16}_{-0.09}$	$-5.31^{+0.22}_{-0.21}$	$-6.56^{+0.13}_{-0.22}$	$-0.20^{+0.14}_{-0.09}$	$0.51^{+0.12}_{-0.07}$
WISE-J105257	$768.40^{+13.94}_{-9.22}$	$4.36^{+0.40}_{-0.38}$	$1.04^{+0.07}_{-0.07}$	$-3.61^{+0.13}_{-0.12}$	$-3.59^{+0.18}_{-0.17}$	$-4.89^{+0.21}_{-0.20}$	$-7.09^{+0.06}_{-0.06}$	$-0.43^{+0.16}_{-0.15}$	$0.77^{+0.13}_{-0.12}$
WISE-J1457	$768.75^{+5.59}_{-10.00}$	$4.67^{+0.23}_{-0.39}$	$1.38^{+0.22}_{-0.19}$	$-3.65^{+0.12}_{-0.14}$	$-3.59^{+0.12}_{-0.18}$	$-4.80^{+0.13}_{-0.24}$	$-6.99^{+0.10}_{-0.09}$	$-0.44^{+0.12}_{-0.16}$	$0.83^{+0.15}_{-0.15}$
2MASS-J1217	$775.64^{+27.09}_{-12.75}$	$4.82^{+0.17}_{-0.28}$	$1.30^{+0.12}_{-0.12}$	$-3.42^{+0.09}_{-0.10}$	$-3.26^{+0.09}_{-0.12}$	$-4.59^{+0.10}_{-0.15}$	$-6.83^{+0.09}_{-0.07}$	$-0.16^{+0.10}_{-0.10}$	$1.03^{+0.15}_{-0.15}$
WISE-J1322	$775.78^{+6.91}_{-19.53}$	$3.87^{+0.77}_{-0.48}$	$1.17^{+0.33}_{-0.22}$	$-3.73^{+0.27}_{-0.23}$	$-3.83^{+0.36}_{-0.25}$	$-5.38^{+0.44}_{-0.52}$	$-6.94^{+0.17}_{-0.17}$	$-0.59^{+0.32}_{-0.23}$	$0.62^{+0.27}_{-0.18}$

WISE-J0223	$787.96^{+4.11}_{-4.60}$	$5.23^{+0.18}_{-0.33}$	$0.81^{+0.09}_{-0.10}$	$-3.12^{+0.11}_{-0.13}$	$-3.25^{+0.09}_{-0.15}$	$-4.72^{+0.15}_{-0.26}$	$-6.80^{+0.09}_{-0.10}$	$-0.02^{+0.10}_{-0.14}$	$0.54^{+0.08}_{-0.07}$
Gliese 570D	$789.90^{+4.05}_{-12.67}$	$5.14^{+0.14}_{-0.26}$	$0.95^{+0.09}_{-0.11}$	$-3.27^{+0.09}_{-0.09}$	$-3.25^{+0.08}_{-0.12}$	$-4.58^{+0.10}_{-0.21}$	$-6.81^{+0.08}_{-0.07}$	$-0.02^{+0.10}_{-0.10}$	$0.77^{+0.08}_{-0.10}$
WISE-PCJ2157	$792.95^{+12.10}_{-9.11}$	$5.22^{+0.15}_{-0.25}$	$0.83^{+0.05}_{-0.05}$	$-3.27^{+0.07}_{-0.08}$	$-3.22^{+0.07}_{-0.12}$	$-4.57^{+0.10}_{-0.15}$	$-6.89^{+0.06}_{-0.06}$	$-0.02^{+0.07}_{-0.10}$	$0.85^{+0.06}_{-0.07}$
WISE-PAJ1711	$805.55^{+2.76}_{-1.80}$	$4.80^{+0.27}_{-0.43}$	$1.17^{+0.23}_{-0.15}$	$-3.45^{+0.14}_{-0.18}$	$-3.40^{+0.14}_{-0.21}$	$-4.74^{+0.14}_{-0.24}$	$-7.05^{+0.11}_{-0.12}$	$-0.24^{+0.14}_{-0.19}$	$0.82^{+0.15}_{-0.14}$
WISE-PCJ2209	$809.34^{+5.18}_{-4.03}$	$5.00^{+0.21}_{-0.30}$	$0.90^{+0.05}_{-0.04}$	$-3.37^{+0.08}_{-0.12}$	$-3.54^{+0.10}_{-0.14}$	$-4.79^{+0.13}_{-0.19}$	$-6.95^{+0.06}_{-0.06}$	$-0.28^{+0.10}_{-0.13}$	$0.50^{+0.05}_{-0.05}$
WISE-J0241	$835.78^{+3.82}_{-4.32}$	$4.90^{+0.19}_{-0.22}$	$1.06^{+0.05}_{-0.05}$	$-3.55^{+0.08}_{-0.08}$	$-3.51^{+0.09}_{-0.10}$	$-4.74^{+0.11}_{-0.12}$	$-6.93^{+0.05}_{-0.04}$	$-0.36^{+0.09}_{-0.09}$	$0.82^{+0.07}_{-0.07}$
WISE-J1124	$848.44^{+26.25}_{-9.67}$	$4.78^{+0.23}_{-0.26}$	$0.99^{+0.10}_{-0.07}$	$-3.41^{+0.10}_{-0.11}$	$-3.45^{+0.11}_{-0.12}$	$-4.68^{+0.15}_{-0.15}$	$-6.75^{+0.09}_{-0.10}$	$-0.25^{+0.12}_{-0.11}$	$0.83^{+0.07}_{-0.08}$
WISE-J2213	$852.44^{+11.78}_{-11.13}$	$4.65^{+0.33}_{-0.28}$	$0.96^{+0.09}_{-0.06}$	$-3.50^{+0.10}_{-0.09}$	$-3.57^{+0.14}_{-0.13}$	$-4.86^{+0.20}_{-0.16}$	$-6.73^{+0.07}_{-0.08}$	$-0.36^{+0.12}_{-0.11}$	$0.63^{+0.12}_{-0.08}$
WISE-J2226	$868.13^{+18.55}_{-13.44}$	$5.27^{+0.18}_{-0.27}$	$0.78^{+0.09}_{-0.06}$	$-3.02^{+0.11}_{-0.15}$	$-2.98^{+0.11}_{-0.14}$	$-4.85^{+0.24}_{-0.37}$	$-6.48^{+0.09}_{-0.14}$	$0.16^{+0.11}_{-0.14}$	$0.82^{+0.14}_{-0.10}$
SDSS-1504	$872.47^{+5.04}_{-9.67}$	$4.98^{+0.12}_{-0.20}$	$1.22^{+0.08}_{-0.07}$	$-3.55^{+0.06}_{-0.08}$	$-3.45^{+0.06}_{-0.10}$	$-4.63^{+0.07}_{-0.11}$	$-6.93^{+0.05}_{-0.05}$	$-0.32^{+0.07}_{-0.09}$	$0.91^{+0.08}_{-0.08}$
WISE-PAJ0123	$872.83^{+3.15}_{-3.97}$	$5.15^{+0.11}_{-0.15}$	$1.02^{+0.07}_{-0.06}$	$-3.51^{+0.07}_{-0.08}$	$-3.48^{+0.07}_{-0.08}$	$-4.59^{+0.06}_{-0.08}$	$-6.78^{+0.06}_{-0.06}$	$-0.31^{+0.09}_{-0.08}$	$0.80^{+0.07}_{-0.06}$
WISE-J1254	$875.62^{+6.77}_{-23.90}$	$3.81^{+0.46}_{-0.28}$	$0.95^{+0.26}_{-0.13}$	$-3.80^{+0.19}_{-0.19}$	$-4.02^{+0.21}_{-0.16}$	$-5.36^{+0.28}_{-0.46}$	$-6.66^{+0.17}_{-0.18}$	$-0.75^{+0.19}_{-0.18}$	$0.41^{+0.19}_{-0.11}$
WISE-J0040	$885.44^{+18.84}_{-13.25}$	$4.66^{+0.34}_{-0.34}$	$0.97^{+0.10}_{-0.09}$	$-3.51^{+0.34}_{-0.11}$	$-3.54^{+0.15}_{-0.15}$	$-4.82^{+0.21}_{-0.19}$	$-6.91^{+0.09}_{-0.08}$	$-0.35^{+0.14}_{-0.13}$	$0.70^{+0.11}_{-0.11}$
WISE-J0521	$880.60^{+4.15}_{-3.15}$	$4.18^{+0.39}_{-0.28}$	$0.85^{+0.03}_{-0.05}$	$-3.47^{+0.15}_{-0.08}$	$-3.54^{+0.19}_{-0.12}$	$-5.07^{+0.14}_{-0.21}$	$-6.79^{+0.07}_{-0.06}$	$-0.27^{+0.18}_{-0.10}$	$0.63^{+0.09}_{-0.08}$
PSO-J224	$892.88^{+8.55}_{-25.81}$	$3.64^{+0.25}_{-0.14}$	$0.91^{+0.07}_{-0.06}$	$-3.86^{+0.09}_{-0.09}$	$-3.92^{+0.12}_{-0.08}$	$-5.25^{+0.13}_{-0.11}$	$-6.89^{+0.08}_{-0.08}$	$-0.62^{+0.16}_{-0.10}$	$0.68^{+0.09}_{-0.08}$
WISE-J0325	$897.80^{+7.93}_{-3.47}$	$3.54^{+0.13}_{-0.08}$	$0.94^{+0.06}_{-0.05}$	$-3.77^{+0.07}_{-0.07}$	$-4.00^{+0.07}_{-0.06}$	$-5.47^{+0.11}_{-0.12}$	$-6.84^{+0.08}_{-0.08}$	$-0.69^{+0.14}_{-0.07}$	$0.47^{+0.09}_{-0.05}$
WISE-J0614	$897.89^{+4.22}_{-14.69}$	$4.93^{+0.12}_{-0.20}$	$1.22^{+0.09}_{-0.09}$	$-3.48^{+0.07}_{-0.07}$	$-3.45^{+0.07}_{-0.09}$	$-4.68^{+0.08}_{-0.11}$	$-6.86^{+0.06}_{-0.05}$	$-0.29^{+0.07}_{-0.08}$	$0.79^{+0.07}_{-0.07}$
2MASS-J1553	$900.88^{+2.03}_{-1.83}$	$4.56^{+0.20}_{-0.20}$	$1.13^{+0.06}_{-0.06}$	$-3.38^{+0.08}_{-0.08}$	$-3.49^{+0.09}_{-0.09}$	$-5.06^{+0.13}_{-0.21}$	$-6.60^{+0.06}_{-0.14}$	$-0.27^{+0.09}_{-0.09}$	$0.58^{+0.05}_{-0.06}$
WISE-J2340	$904.21^{+5.96}_{-5.98}$	$4.72^{+0.17}_{-0.23}$	$1.47^{+0.14}_{-0.11}$	$-3.58^{+0.09}_{-0.10}$	$-3.56^{+0.09}_{-0.11}$	$-4.87^{+0.10}_{-0.15}$	$-6.73^{+0.08}_{-0.08}$	$-0.40^{+0.10}_{-0.11}$	$0.78^{+0.09}_{-0.08}$
WISEPA J1852	$915.71^{+14.64}_{-5.53}$	$5.12^{+0.22}_{-0.28}$	$0.80^{+0.10}_{-0.05}$	$-3.16^{+0.12}_{-0.15}$	$-3.06^{+0.13}_{-0.15}$	$-4.62^{+0.14}_{-0.20}$	$-6.38^{+0.09}_{-0.13}$	$0.06^{+0.13}_{-0.16}$	$0.93^{+0.16}_{-0.12}$
SDSS-J16283	$916.45^{+6.58}_{-10.41}$	$4.91^{+0.31}_{-0.40}$	$0.83^{+0.07}_{-0.06}$	$-3.29^{+0.12}_{-0.13}$	$-3.28^{+0.15}_{-0.18}$	$-4.76^{+0.20}_{-0.22}$	$-6.58^{+0.09}_{-0.09}$	$-0.11^{+0.14}_{-0.16}$	$0.73^{+0.13}_{-0.10}$
WISE-J2348	$921.60^{+1.08}_{-9.23}$	$4.94^{+0.29}_{-0.32}$	$0.77^{+0.20}_{-0.07}$	$-3.28^{+0.17}_{-0.17}$	$-3.20^{+0.17}_{-0.15}$	$-4.74^{+0.19}_{-0.22}$	$-6.51^{+0.15}_{-0.27}$	$-0.07^{+0.17}_{-0.16}$	$0.87^{+0.23}_{-0.13}$
2MASS-J0050	$945.64^{+5.83}_{-12.09}$	$5.26^{+0.22}_{-0.19}$	$0.75^{+0.05}_{-0.04}$	$-3.19^{+0.10}_{-0.12}$	$-3.07^{+0.11}_{-0.14}$	$-4.49^{+0.12}_{-0.13}$	$-6.37^{+0.08}_{-0.09}$	$0.10^{+0.11}_{-0.12}$	$0.98^{+0.11}_{-0.10}$
2MASS-J0727	$953.07^{+3.34}_{-1.80}$	$5.23^{+0.17}_{-0.20}$	$0.76^{+0.05}_{-0.04}$	$-3.09^{+0.10}_{-0.09}$	$-3.15^{+0.10}_{-0.10}$	$-4.76^{+0.10}_{-0.26}$	$-6.51^{+0.08}_{-0.10}$	$0.05^{+0.10}_{-0.10}$	$0.65^{+0.07}_{-0.06}$

APPENDIX B

BEST-FIT SPECTRA OF ALL 50 T-DWARFS

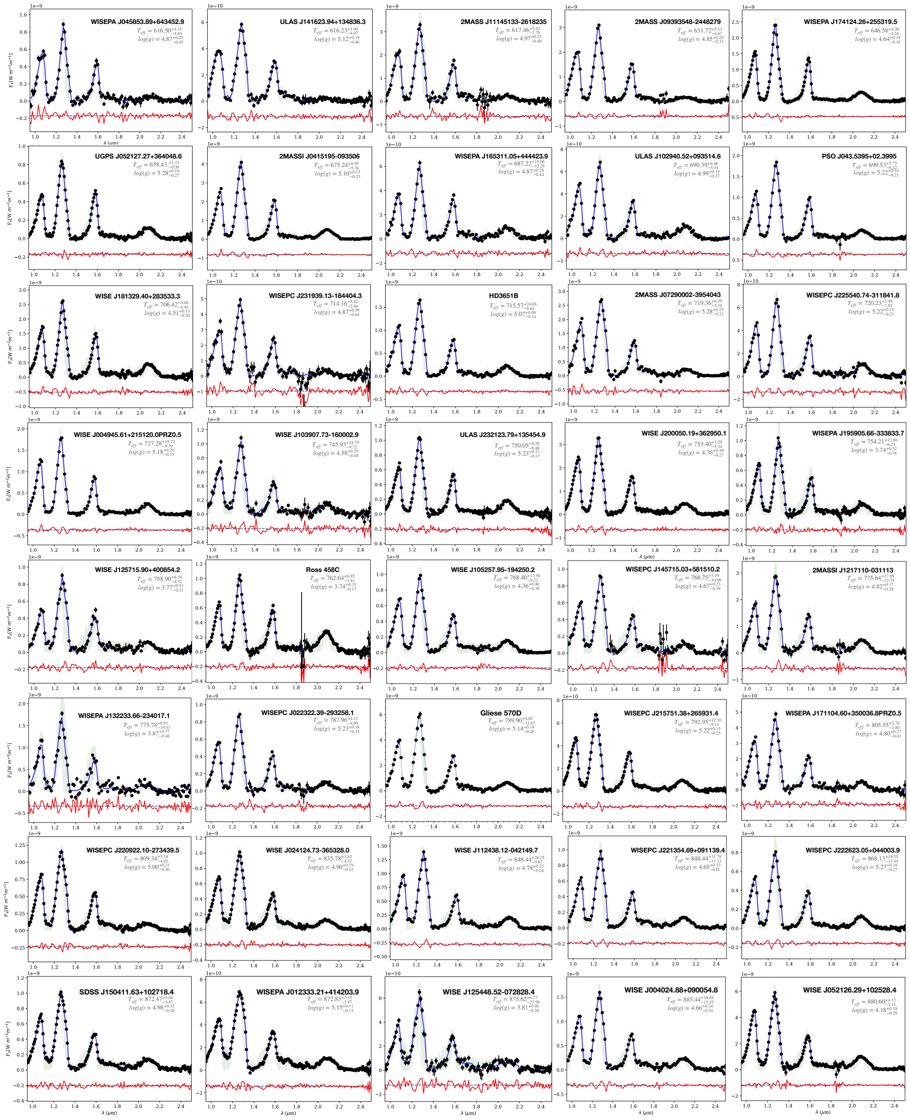
WISEPA J045853.89+643452.9
$T_{eff} = 616.50^{+4.15}_{-9.05}$
$log(g) = 4.87^{+0.25}_{-0.45}$
ULAS J141623.94+134836.3
$T_{eff} = 616.23^{+1.90}_{-4.07}$
$log(g) = 5.12^{+0.19}_{-0.46}$
2MASS J11145133-2618235
$T_{eff} = 617.46^{+5.43}_{-2.78}$
$log(g) = 4.97^{+0.22}_{-0.40}$
2MASS J09393548-2448279
$T_{eff} = 631.72^{+5.13}_{-6.67}$
$log(g) = 4.85^{+0.29}_{-0.33}$
WISEPA J174124.26+255319.5
$T_{eff} = 646.58^{+4.26}_{-4.58}$
$log(g) = 4.64^{+0.18}_{-0.18}$
UGPS J052127.27+364048.6
$T_{eff} = 658.43^{+1.21}_{-0.58}$
$log(g) = 5.28^{+0.19}_{-0.27}$
2MASSI J0415195-093506
$T_{eff} = 675.24^{+8.95}_{-5.38}$
$log(g) = 5.10^{+0.15}_{-0.25}$
WISEPA J165311.05+444423.9
$T_{eff} = 687.22^{+15.06}_{-12.25}$
$log(g) = 4.87^{+0.28}_{-0.44}$
ULAS J102940.52+093514.6
$T_{eff} = 690.39^{+6.46}_{-3.34}$
$log(g) = 4.99^{+0.19}_{-0.27}$
PSO J043.5395+02.3995
$T_{eff} = 699.53^{+5.75}_{-6.22}$
$log(g) = 5.22^{+0.14}_{-0.21}$
WISE J181329.40+283533.3
$T_{eff} = 706.42^{+4.04}_{-4.45}$
$log(g) = 4.51^{+0.13}_{-0.20}$
WISEPC J231939.13-184404.3
$T_{eff} = 714.16^{+5.82}_{-2.84}$
$log(g) = 4.87^{+0.59}_{-0.64}$
HD3651B
$T_{eff} = 715.57^{+24.68}_{-9.65}$
$log(g) = 5.07^{+0.09}_{-0.14}$
2MASS J07290002-3954043
$T_{eff} = 719.36^{+6.39}_{-5.10}$
$log(g) = 5.28^{+0.15}_{-0.23}$
WISEPC J225540.74-311841.8
$T_{eff} = 720.23^{+3.48}_{-7.03}$
$log(g) = 5.22^{+0.15}_{-0.23}$
WISE J004945.61+215120.0PRZ0.5
$T_{eff} = 727.28^{+19.72}_{-9.70}$
$log(g) = 5.18^{+0.20}_{-0.33}$
WISE J103907.73-160002.9
$T_{eff} = 745.93^{+24.79}_{-9.72}$
$log(g) = 4.58^{+0.29}_{-0.48}$
ULAS J232123.79+135454.9
$T_{eff} = 750.05^{+8.29}_{-8.48}$
$log(g) = 5.23^{+0.11}_{-0.17}$
WISE J200050.19+362950.1
$T_{eff} = 753.40^{+3.29}_{-5.34}$
$log(g) = 4.76^{+0.39}_{-0.27}$
WISEPA J195905.66-333833.7
$T_{eff} = 754.21^{+17.80}_{-6.23}$
$log(g) = 3.74^{+0.32}_{-0.18}$
WISE J125715.90+400854.2
$T_{eff} = 758.90^{+6.54}_{-4.72}$
$log(g) = 3.77^{+0.51}_{-0.21}$
Ross 458C
$T_{eff} = 762.64^{+6.85}_{-1.81}$
$log(g) = 3.74^{+0.33}_{-0.17}$
WISE J105257.95-194250.2
$T_{eff} = 768.40^{+13.94}_{-9.22}$
$log(g) = 4.36^{+0.40}_{-0.38}$
WISEPC J145715.03+581510.2
$T_{eff} = 768.75^{+5.59}_{-10.00}$
$log(g) = 4.67^{+0.23}_{-0.39}$
2MASSI J1217110-031113
$T_{eff} = 775.64^{+27.09}_{-12.75}$
$log(g) = 4.82^{+0.17}_{-0.28}$
WISEPA J132233.66-234017.1
$T_{eff} = 775.78^{+6.91}_{-19.53}$
$log(g) = 3.87^{+0.77}_{-0.48}$
WISEPC J022322.39-293258.1
$T_{eff} = 787.96^{+4.11}_{-4.60}$
$log(g) = 5.23^{+0.18}_{-0.33}$
Gliese 570D
$T_{eff} = 789.90^{+4.05}_{-12.67}$
$log(g) = 5.14^{+0.14}_{-0.26}$
WISEPC J215751.38+265931.4
$T_{eff} = 792.95^{+12.10}_{-9.11}$
$log(g) = 5.22^{+0.15}_{-0.25}$
WISEPA J171104.60+350036.8PRZ0.5
$T_{eff} = 805.55^{+2.76}_{-1.80}$
$log(g) = 4.80^{+0.27}_{-0.43}$
WISEPC J220922.10-273439.5
$T_{eff} = 809.34^{+5.18}_{-4.03}$
$log(g) = 5.00^{+0.21}_{-0.30}$
WISE J024124.73-365328.0
$T_{eff} = 835.78^{+3.83}_{-4.32}$
$log(g) = 4.90^{+0.19}_{-0.22}$
WISE J112438.12-042149.7
$T_{eff} = 848.44^{+26.25}_{-9.67}$
$log(g) = 4.78^{+0.23}_{-0.26}$
WISEPC J221354.69+091139.4
$T_{eff} = 848.44^{+11.78}_{-11.13}$
$log(g) = 4.65^{+0.33}_{-028.}$
WISEPC J222623.05+044003.9
$T_{eff} = 868.13^{+18.55}_{-13.44}$
$log(g) = 5.27^{+0.18}_{-0.27}$
SDSS J150411.63+102718.4
$T_{eff} = 872.47^{+5.04}_{-9.67}$
$log(g) = 4.98^{+0.12}_{-0.20}$
WISEPA J012333.21+414203.9
$T_{eff} = 872.83^{+3.15}_{-3.97}$
$log(g) = 5.15^{+0.11}_{-0.15}$
WISE J125448.52-072828.4
$T_{eff} = 875.62^{+6.77}_{-23.90}$
$log(g) = 3.81^{+0.46}_{-0.28}$
WISE J004024.88+090054.8
$T_{eff} = 885.44^{+18.84}_{-13.25}$
$log(g) = 4.66^{+0.34}_{-0.34}$
WISE J052126.29+102528.4
$T_{eff} = 880.60^{+4.15}_{-3.15}$
$log(g) = 4.18^{+0.39}_{-0.28}$
$F_\lambda [W\ m^{-2} m^{-1}]$
λ (μm)

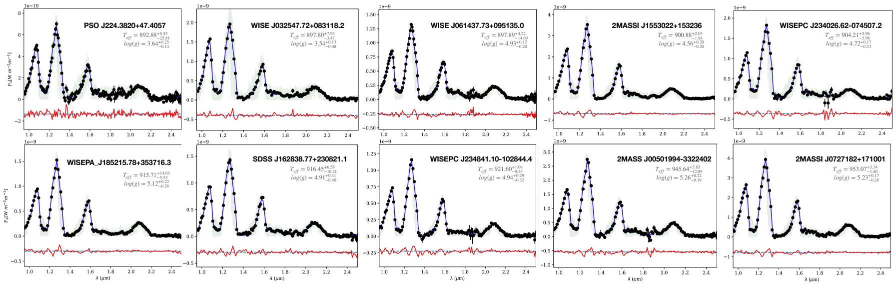
PSO J224.3820+47.4057
$T_{eff} = 892.88^{+8.55}_{-25.81}$
$log(g) = 3.64^{+0.25}_{-0.14}$
WISE J032547.72+083118.2
$T_{eff} = 897.80^{+7.93}_{-3.47}$
$log(g) = 3.54^{+0.13}_{-0.08}$
WISE J061437.73+095135.0
$T_{eff} = 897.89^{+4.22}_{-14.69}$
$log(g) = 4.93^{+0.12}_{-0.20}$
2MASSI J1553022+153236
$T_{eff} = 900.88^{+2.03}_{-1.84}$
$log(g) = 4.56^{+0.20}_{-0.20}$
WISEPC J234026.62-074507.2
$T_{eff} = 904.21^{+5.96}_{-5.98}$
$log(g) = 4.72^{+0.17}_{-0.23}$
WISEPA_J185215.78+353716.3
$T_{eff} = 915.71^{+14.64}_{-5.53}$
$log(g) = 5.12^{+0.22}_{-0.28}$
SDSS J162838.77+230821.1
$T_{eff} = 916.45^{+6.58}_{-10.41}$
$log(g) = 4.91^{+0.31}_{-0.40}$
WISEPC J234841.10-102844.4
$T_{eff} = 921.60^{+1.08}_{-9.23}$
$log(g) = 4.94^{+0.29}_{-0.32}$
2MASS J00501994-3322402
$T_{eff} = 945.64^{+5.83}_{-12.09}$
$log(g) = 5.26^{+0.22}_{-0.19}$
2MASSI J0727182+171001
$T_{eff} = 953.07^{+3.34}_{-1.80}$
$log(g) = 5.23^{+0.17}_{-0.20}$
$F_\lambda [W\ m^{-2} m^{-1}]$
λ (μm)
1e−10
1e−9

Figure B.1:

APPENDIX C

THERMAL PROFILES OF ALL 50 OBJECTS

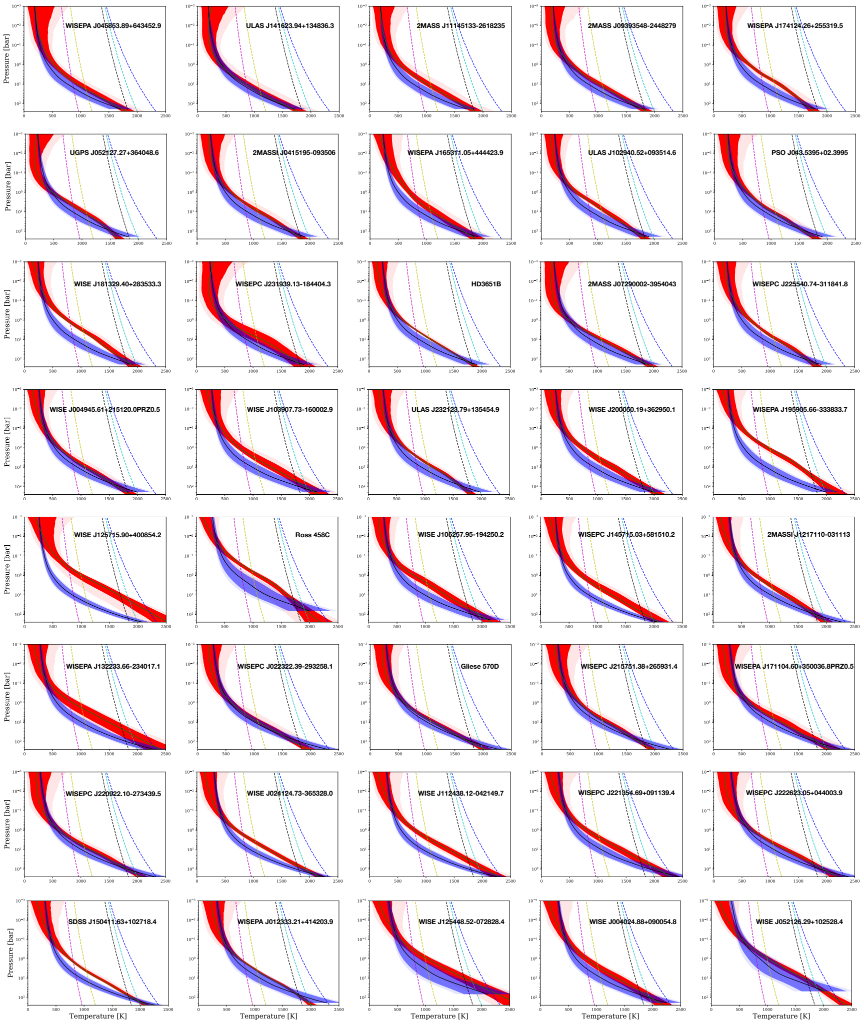
WISEPA J045853.89+643452.9
ULAS J141623.94+134836.3
2MASS J11145133-2618235
2MASS J09393548-2448279
WISEPA J174124.26+255319.5
UGPS J052127.27+364048.6
2MASSI J0415195-093506
WISEPA J165311.05+444423.9
ULAS J102940.52+093514.6
PSO J043.5395+02.3995
WISE J181329.40+283533.3
WISEPC J231939.13-184404.3
HD3651B
2MASS J07290002-3954043
WISEPC J225540.74-311841.8
WISE J004945.61+215120.0PRZ0.5
WISE J103907.73-160002.9
ULAS J232123.79+135454.9
WISE J200050.19+362950.1
WISEPA J195905.66-333833.7
WISE J125715.90+400854.2
Ross 458C
WISE J105257.95-194250.2
WISEPC J145715.03+581510.2
2MASSI J1217110-031113
WISEPA J132233.66-234017.1
WISEPC J022322.39-293258.1
Gliese 570D
WISEPC J215751.38+265931.4
WISEPA J171104.60+350036.8PRZ0.5
WISEPC J220922.10-273439.5
WISE J024124.73-365328.0
WISE J112438.12-042149.7
WISEPC J221354.69+091139.4
WISEPC J222623.05+044003.9
SDSS J150411.63+102718.4
WISEPA J012333.21+414203.9
WISE J125448.52-072828.4
WISE J004024.88+090054.8
WISE J052126.29+102528.4
Pressure [bar]
Temperature [K]
0
500
1000
1500
2000
2500
10^{-3}
10^{-2}
10^{-1}
10^{0}
10^{1}
10^{2}

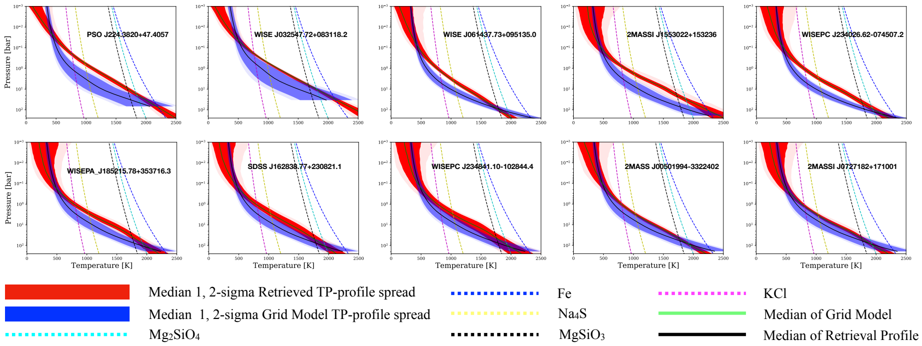
PSO J224.3820+47.4057
WISE J032547.72+083118.2
WISE J061437.73+095135.0
2MASSI J1553022+153236
WISEPC J234026.62-074507.2
WISEPA_J185215.78+353716.3
SDSS J162838.77+230821.1
WISEPC J234841.10-102844.4
2MASS J00501994-3322402
2MASSI J0727182+171001
Pressure [bar]
Temperature [K]
0
500
1000
1500
2000
2500
10^{-3}
10^{-2}
10^{-1}
10^{0}
10^{1}
10^{2}
Median 1, 2-sigma Retrieved TP-profile spread
Median 1, 2-sigma Grid Model TP-profile spread
Mg_2SiO_4
Fe
Na_4S
$MgSiO_3$
KCl
Median of Grid Model
Median of Retrieval Profile

Figure C.1: